

Angular Diameters of Stars from the Mark III Optical Interferometer

D. Mozurkewich, J. T. Armstrong¹ and R. B. Hindsley

Naval Research Laboratory, 4555 Overlook Ave. SE, Washington, DC 20375

A. Quirrenbach¹

Sterrewacht Leiden, Postbus 9513, NL-2300 RA Leiden, The Netherlands

C. A. Hummel¹, D. J. Hutter, K. J. Johnston, A. R. Hajian

U. S. Naval Observatory, 3450 Massachusetts Ave. NW, Washington DC 20392

Nicholas M. Elias II²

Ball Aerospace & Technologies Corp., Terrestrial Planet Finder Program, PO Box 1062, Boulder, CO 80306-1062

D. F. Buscher¹

Astrophysics Group, Cavendish Laboratory, Cambridge CB3 0HE, United Kingdom

and

R. S. Simon³

National Radio Astronomy Observatory, Edgemont Rd., Charlottesville, VA 22903

ABSTRACT

Observations of 85 stars were obtained at wavelengths between 451 nm and 800 nm with the Mark III Stellar Interferometer on Mount Wilson, near Pasadena, CA. Angular diameters were determined by fitting a uniform-disk model to the visibility amplitude versus projected baseline length. Half the angular diameters determined at 800 nm have formal errors smaller than 1 percent. Limb-darkened angular diameters, effective temperatures and surface brightnesses were determined for these stars and relationships between these parameters are presented. Scatter in these relationships is larger than would be expected from the measurement uncertainties. We argue that this scatter is not due to an underestimate of the angular diameter errors; whether it is due to

¹Formerly at Universities Space Research Association, 300 D St. SW, Washington DC 20024

²Formerly U. S. Naval Observatory, 3450 Massachusetts Ave. NW, Washington DC 20392

³Formerly at Naval Research Laboratory, 4555 Overlook Avenue SE, Washington, DC 20375

photometric errors or is intrinsic to the relationship is unresolved. The agreement with other observations of the same stars at the same wavelengths is good; the width of the difference distribution is comparable to that estimated from the error bars, but the wings of the distribution are larger than Gaussian. Comparison with infrared measurements is more problematic; in disagreement with models, cooler stars appear systematically smaller in the near-infrared than expected; warmer stars larger.

Subject headings: stars: fundamental parameters — stars: atmospheres

1. Introduction

Measuring angular diameters is necessary for understanding the fundamental properties of stars. An important application is in the direct determination of effective temperatures. Stellar atmosphere models are parameterized in terms of effective temperature, requiring an empirical determination of effective temperatures for a direct comparison of observations to theory. Since extensive diameter observations have been lacking, indirect methods of determining effective temperatures have been used. Currently, the method of choice is the infrared flux method first advocated by Blackwell & Shallis (1977).

Effective temperatures can be difficult to determine because they require knowledge of the bolometric flux corrected for interstellar extinction. Barnes & Evans (1976) showed that there is a tight relationship between surface brightness and photometric color so that the magnitude and color of a star can be used to estimate its angular diameter. The reddening curve is nearly parallel to this relationship so that accurate extinction corrections are not required for estimating angular diameters. Recently, there has been interest in this technique for calibrating the Cepheid distance scale (Fouqué & Gieren 1997).

Another need for high quality angular diameter measurements is as a test of model stellar atmospheres. These models are normally used to predict stellar spectra, and although they are solidly based on the laws of physics, the models contain enough approximations (e.g. convection, extended atmospheres and spots) and enough poorly known physical parameters (e.g. opacity, line strengths) that they are effectively fit to the stellar spectra they are trying to predict. With the data presented here, we finally have enough measured angular diameters covering a wide enough wavelength range to provide constraints on the model atmospheres through their limb-darkening predictions. As we will see later in this paper, the observations are not entirely consistent with those predictions, although the discrepancies are small enough that it may still be possible to attribute them to the observations if systematic effects are larger than they appear.

Most empirical angular diameter data have come in small sets. Different sets were often obtained with different observational techniques so that direct comparisons are difficult. More importantly, the published diameters were obtained at several wavelengths, and data taken at

different wavelengths can be compared only if the limb darkening, or at least its variation with wavelength is known. There are very few direct observations of limb darkening or tests of its wavelength dependence.

We present 220 angular diameter measurements of 85 stars obtained between 1988 and 1990, representing one of the largest single collections of directly measured stellar angular diameters. The observations were made at $\lambda\lambda$ 800, 550, 500 and 451 nm, allowing us to measure the wavelength dependence of limb darkening through the visible. We compare other observations at similar wavelengths for consistency and between wavelengths to study limb darkening.

This paper incorporates most of the stellar diameters measured with the Mark III, including the data from Mozurkewich et al. (1991). It does not include data for Mira (Quirrenbach et al. 1992), carbon stars (Quirrenbach et al. 1994a), and red giants observed in a TiO band and the adjacent continuum (Quirrenbach et al. 1993). Finally, we have no new observations of α Ori (Mozurkewich et al. 1991), so do we not repeat that result here.

2. Observations

The Mark III Stellar Interferometer was a joint project of the Naval Research Laboratory, the US Naval Observatory, the Smithsonian Astrophysical Observatory, and MIT, and was located on Mount Wilson, near Pasadena, California (Shao et al. 1988a). The Mark III was designed primarily for wide angle astrometry, and consisted initially of three 5-cm apertures used in pairs, with baseline lengths of 12 meters. First stellar fringes with these astrometric elements were detected in 1986.

Although the fundamental measurement for astrometry is the fringe delay, visibility (fringe) amplitude measurements were also successful, particularly for determining binary star separations and stellar angular diameters. In 1988, two additional apertures on a variable length baseline (20 baseline lengths from 3 to 31.5 m) were added, intended exclusively for these visibility measurements. All of the observations presented here were obtained with the variable baseline. The Mark III was decommissioned in December 1992.

The Mark III used a delay modulation technique for detecting and tracking fringes. The modulation was one wavelength in amplitude; photon counts were recorded in four quarter-wavelength bins and used to determine the square of the fringe visibility amplitude, V^2 , the fundamental datum for determining stellar characteristics with a single-baseline optical interferometer. Observations were made simultaneously in four bands, a broad band ($\lambda \approx 700$ nm, $\Delta\lambda \approx 300$ nm) for fringe tracking and three narrow ($\Delta\lambda \approx 20 - 25$ nm) filters for science data. For all of the observations reported here, the science bands had center wavelengths of 800, 550, and either 500 or 451 nm.

The data described in this paper consist of more than 15000 visibility amplitude measurements obtained during 133 nights between 1988 September 17 and 1990 October 15. A typical night consisted of 100 to 200 scans, each 75 seconds long, with 10 to 20 stars in the observing list, with

the time evenly divided between program stars and calibration stars. Three to ten scans were obtained on each program star on each night. Because changing baselines required from two to four hours, each night’s data consisted only of observations on a single baseline.

The program star observations are summarized in Table 1. The first column identifies the star. The column labeled Days shows the number of nights on which the star was observed. The remaining columns list, for each star, the number of scans at each of the 20 baseline lengths.

The data presented here were taken and reduced using the techniques discussed by Mozurkewich et al. (1991). For each scan, we calculated the average V^2 and its formal error, estimated from its variation during the scan. Because most instrumental and atmospheric effects become more severe at shorter wavelengths, the 800 nm data were consistently the highest quality despite the higher angular resolution at the shorter wavelengths.

3. Calibration

Observations of the calibration stars were used to generate a multiplicative correction for the instrumental and atmospheric reduction of V^2 . This calibration generally consisted of three parts: a quadratic dependence on zenith angle, a quadratic dependence on a seeing parameter determined from the interferometer, and a slowly varying function of time. The time dependence was modeled either as a low order polynomial or a boxcar smoothing function. The calibration stars were chosen to be small, relative to the program stars, and to have roughly the same sky coverage. This produced a single calibration function that was used for all stars for the entire night.

The true errors were always larger than the formal errors due to the presence of unmodeled systematics. We estimated the size of this effect by calculating the χ^2 per degree of freedom, χ^2_ν , of the calibration scans with respect to the calibration function. We added a calibration error to the formal errors in quadrature and adjusted the calibration error until the χ^2_ν of the calibration was equal to one. Thus a single calibration error was estimated for each night and wavelength. A typical value for the 800 nm data was 1%.

This calibration procedure makes the implicit assumption that any degradation of V^2 due to the atmosphere or the instrument is purely multiplicative. This assumption is justified on both theoretical and observational grounds. The only potential source of an additive bias is that introduced by detection statistics. The detectors were photomultiplier tubes operated in photon counting mode. The photon counts have a Poisson distribution for which the bias is easily calculated. Quirrenbach et al. (1994b) were unable to detect an additive offset in our V^2 measurements and set an upper limit of 1×10^{-4} , significantly smaller than any measurement errors quoted in this paper. Therefore, we can safely assume that additive terms are negligible.

4. Uniform-disk Model Fitting: Results and Uncertainties

4.1. Model Fits

Determining angular diameters from the observed squared visibility amplitudes requires knowledge of the star’s intensity distribution. Since in general stellar limb-darkening profiles have not been measured, stellar models must be used to determine these profiles. However, fitting the data with a limb-darkened disk mixes the uncertainties of the model with the uncertainties due to the data. Traditionally this problem is solved by using a uniform-disk model. After a uniform-disk diameter has been determined, it is converted into a more realistic limb-darkened diameter. When applicable, this approach has the advantage of nicely separating the fit to the data, embodied in the uniform-disk diameter, from model dependent assumptions about the limb darkening, contained in the limb-darkening conversion. Since all the data presented here sample spatial frequencies lower than that needed to reach the first zero of the visibility function, a uniform disk fits the data well and this approach is adequate for the data presented here.

We fit V^2 as a function of projected baseline length, B , using a uniform-disk model for the stellar intensity distribution

$$V^2 = \left| \frac{2 V_0 J_1(\pi \theta_{UD} B / \lambda)}{\pi \theta_{UD} B / \lambda} \right|^2, \quad (1)$$

where θ_{UD} is the uniform-disk angular diameter of the star. The parameter V_0 , the visibility amplitude at zero spacing, may seem mysterious since the visibility amplitude must be unity at zero baseline. It is used to correct for omissions in the model and to provide a check of the calibration. Omissions in the model occur when the target is a component of a more extended system. For example, the visibility of a binary star with separation θ will oscillate as $\sin(2\pi\theta B/\lambda)$, but because of the finite temporal coherence of the light, this oscillation will damp out after roughly $\lambda/\Delta\lambda$ oscillations. If the shortest baseline is too long to sample this oscillation but short enough for the target star to appear unresolved, the variation of V^2 with baseline will appear to be that of a single star with V_0 reduced to the fraction of the total light from the system originating in the target star. A similar situation occurs when structure of the star has two or more different spatial scales; a star with a circumstellar envelope or an extended atmosphere with a small hot spot are examples. If the baselines are long enough to sample only the smaller structure, V_0 will be the fraction of the total emission originating in the smaller structure. A search of the literature shows that a number of stars discussed in this paper are members of binary star systems.

When just an angular diameter is fit to the data, both θ_{UD} and its uncertainty are constrained primarily by the data on the longest baseline. But when V_0 is allowed to vary, short baselines are also needed not only to constrain V_0 but also to constrain θ_{UD} . It is not the range of baselines that matters; it is the range of visibilities sampled by those baselines that determines whether a two parameter fit is well constrained. Since the advantages of fitting V_0 were not fully appreciated

when the data were taken, some of the stars do not have data covering a sufficient range of visibility amplitudes to allow a two parameter fit.

Treating data at each wavelength for each star separately, we identified 176 data sets of sufficiently quality to constrain V_0 . For these observations, two-parameter fits to Equation 1 were performed. For the remaining 44 data sets, one-parameter fits were used holding $V_0 = 1$. The resulting diameters are shown in Table 2, columns 3 to 6. In the next section, we examine the fitted values of V_0 and argue that this procedure is justified.

4.2. Zero Spacing Visibilities

The values of V_0 determined from the fits are collected in Table 3 and displayed as a histogram in Figure 1. The distribution peaks at the expected value of $V_0 = 1.0$ but has a significant tail toward low V_0 . We interpret this distribution as a combination of two parent populations: a symmetric one peaked at $V_0 = 1.0$ showing the random errors associated with our estimate of V_0 and a tail to low values showing the need for a more complicated model for some of the stars.

To test this assertion, we identified the 17 stars in our sample which are known to have companions based on the “Multiflag” identifier in the Hipparcos Catalog (1997). For each of these stars, Table 3 gives an estimate of V_0 based on what we could glean from the literature about the companions.

Although these estimates are crude, it is encouraging to see reasonably good agreement between the estimated and measured values. These stars are also indicated in Figure 1 with hatched symbols. The remaining low V_0 point is μ Cep, a very-luminous supergiant which may be expected to show significant departures from a uniform-disk model.

Since we are unaware of any other binary systems in our sample, we are justified holding $V_0 = 1$ when data on short baselines are not available.

4.3. Diameter Error Estimates

The median of the χ_ν^2 for the diameter fits was 1.30 for the 800 nm data, and 1.32 for all wavelengths. This departure from unity implies the formal errors for V^2 , determined from the fluctuations of the visibility within each scan, underestimate the true errors. We compensated for this underestimate by adding a systematic error, $\delta\sigma$, in quadrature with the formal error for V^2 and adjusting $\delta\sigma$ until χ_ν^2 equaled unity. The values of $\delta\sigma$ needed ranged from 0.015 at 800 nm to 0.043 at 451 nm.

We then estimated the diameter uncertainty for each star and wavelength by increasing the angular diameter until χ_ν^2 increased from its minimum value to the 68% confidence level. The

resulting diameter uncertainties for the 800 nm data are between 0.1% and 2.5%, with a median of 0.5%. The median error increases to 0.9% at 550 nm and to 2% at 451 nm, showing roughly the expected quadratic degradation of performance with wavelength.

The ultimate accuracy of the Mark III angular diameters is limited by dozens of systematic effects distributed between the atmosphere, the instrument, and the data reduction. We give two examples here: (1) Differences in the shape of the stellar spectra within the filter bandpasses can shift the effective wavelengths of the filters away from the values determined from the filter transmission curves. An error in the effective wavelength directly affects the angular diameter determined from Equation 1. (2) The limb-darkening conversion was determined by matching the uniform and limb-darkened disk models at $V^2 = 0.3$. Using different values of V^2 at which to match the models result in different conversions. Since the data were taken over a range of baselines, each with a different value of V^2 , the limb-darkening conversion is not well defined.

Because many of these effects give systematic errors of as much as a few tenths of a percent, we have assumed that no errors are less than 1% at 800 nm, 1.4% at 550 and 500 nm and 2% at 451 nm. The adopted errors are listed with the uniform-disk diameters in Table 2, columns 3 to 6.

4.4. Limb-Darkened Diameters

Fitting a limb-darkened stellar profile with a uniform-disk model results in an underestimate of the diameter that increases as the limb darkening increases. We used a multiplicative factor to convert from uniform-disk diameters to limb-darkened diameters. This factor varies from star to star and was calculated by comparing the predicted variation of V^2 with baseline length for both uniform-disk and limb-darkened disk models and determining the ratio of diameters required for the two functions to agree at a value of $V^2 = 0.3$. Although it would be more accurate to fit the limb-darkened model directly to the data, the approach we adopted agrees with the direct fit to within a few parts in 1000, good enough for the data in this paper. We used the quadratic limb-darkening coefficients given by Claret et al. (1995) and Diaz-Cordoves et al. (1995), which were determined from the Kurucz models. These are the only limb-darkening calculations used in this paper.

The limb-darkening coefficients are given as functions of effective temperature and surface gravity, while the observational data are in terms of photometric colors and luminosity classes. The luminosity classes were taken from the Bright Star Catalog (Hoffleit 1990) and the photometry from Johnson et al. (1966). The conversion between these two spaces was performed using the tables in Strizys (1992). The adopted photometric and spectroscopic data for these stars appear in Table 4. The equation converting limb-darkening coefficients and angular diameter to V^2 is given by (Quirrenbach et al. 1996). We corrected the normalization of their Equation 3 to give unit visibility amplitude at zero spacing.

Figure 2 shows the variation of the limb-darkening conversion factor as a function of color for

four wavelengths for giants and main sequence stars. The factors for supergiants are not shown. The supergiant coefficients given by Claret et al. (1995) and Diaz-Cordoves et al. (1995) give factors that follow those of the giants (except for the coolest stars at 800 nm), but these coefficients were calculated for plane parallel atmospheres. A supergiant’s extended atmosphere would increase the limb darkening, although it is not obvious how it would affect the wavelength dependence. The 2.2 μm conversions are included in the figure, since we will be comparing our observations to those from infrared interferometers.

Our 800 nm data are of higher quality than the shorter wavelength data, and the limb-darkening conversion factors are smallest at that wavelength. Smaller factors imply a smaller chance of systematic errors. As a result, we calculated the limb-darkened diameters directly from the measured 800 nm uniform-disk diameters rather than perform a least squares fit to all the data.

5. Comparison with Other Observations

Intensity Interferometer. Hanbury Brown et al. (1974) observed early type stars in the southern hemisphere whereas we primarily observed cooler stars in the northern hemisphere. There are four stars in common. Their observations were at 451 nm, the wavelength where our data is least accurate. The comparison is shown in Table 5. The agreement is similar whether we compare the 451 nm uniform-disk diameters or the limb-darkened diameters. In the limb-darkened comparison, the diameters of three stars are in agreement to better than the expected errors; one star deviates by 3.3 standard deviations in the direction of the Mark III diameter being larger. The comparison of the uniform-disk diameters show differences of 0.6, 1.0, 1.1, and 2.3 standard deviations. This level of agreement implies that our claimed errors are not wildly incorrect, but perhaps slightly underestimated. The star with the largest deviation, α Aql, is a fast rotator. van Belle et al (2001) measured an oblateness large enough to produce a ten percent variation in measured diameter, depending on the orientation of the baseline.

Other Mark III diameters. There are three previous sets of stellar angular diameters from the Mark III. The eleven stars in common with Mozurkewich et al. (1991) are typically in agreement to within a few tenths of a standard deviation. This is not surprising because the same instrument and observing techniques were used in both publications and the earlier data were included in this work.

Earlier data from Hutter et al. (1989) were obtained at 674 nm. Of the 13 stars in common, the median deviation of the limb-darkened angular diameters is 2.3σ . The older measurements give systematically larger angular diameters. These data were taken before we understood the calibration of the system. More importantly, the data were taken using baselines in the range of 8 to 12 meters. Our experience is that observing with more baselines, or at least a larger range of baselines, is necessary if we are to understand the systematics in the data. These comments are also true for the observations in Shao et al. (1988b) where all four of the stars were reported to

have systematically larger angular diameters than those we obtain in this work.

NPOI. Nordgren et al. (1999) published a number of uniform-disk diameters from the NPOI and saw a systematic offset between those diameters and the Mark III diameters. Nordgren et al. (2001) observed additional stars and included limb-darkening conversions to account for the difference in mean wavelength between the two instruments. They did their own conversion for limb-darkening starting from the Mark III uniform-disk diameters. Comparing the NPOI limb-darkened diameters and errors from that paper and the limb-darkened diameters and errors reported here, we see good agreement; of the 39 stars in common between the two data sets, 51% have deviations less than 1σ , 89% agree to better than 2σ and 95% are within 3σ . Two stars disagree by more than 3σ : ν Vir at 3.5σ and η Dra at 3.8σ . We conclude that in general these two instruments agree, and their error estimates are a good representation of the quality of most of the data. At this time, it is not known if the outliers represent elevated wings to the error distributions or if they are due to intrinsic variations in these stars.

Infrared Flux Methods. These angular diameters are determined by comparing observed fluxes with predictions from model atmospheres. There are two approaches: the infrared flux method (IRFM) (Blackwell & Lynas-Gray 1993; Blackwell et al. 1990) uses the ratio of total integrated flux to K -band flux as a temperature indicator. Bell & Gustafsson (1989) compared observed photometry to synthetic colors. We have 23 stars in common with Blackwell et al. (1990), 13 in common with Blackwell & Lynas-Gray (1993) and 20 in common with Bell & Gustafsson (1989), giving a total of 56 diameter estimates of 33 stars. These data are shown in Table 6. Since no errors are quoted for these results, the last column of Table 6 gives the diameter difference in units of the Mark III error. The median fractional difference between the IRFM estimates and the Mark III measurements is 0.3 percent in the direction of the Mark III diameters being larger. The median deviation is 1.2σ , with 68% of the diameters in agreement to within 1.8σ , and 95% within 4σ . As a whole, the agreement is good considering that the uncertainties in the measurements are underestimates. Seven of the measurements differ by more than 3σ and 17 differ by more than 2σ . If we make the reasonable assumption of 2% errors in the IRFM diameters, χ^2_ν is reduced to 1.

6. Effective Temperatures

The effective temperature is defined by the equation

$$L = 4\pi\sigma r^2 T_{\text{EFF}}^4, \quad (2)$$

where σ is the Stephan-Boltzmann constant. Although neither the luminosity, L , stellar radius, r , nor the effective temperature, T_{EFF} , are directly observable, if we divide by the square of the distance, we obtain

$$F_{\text{TOT}} = \sigma(\theta/2)^2 T_{\text{EFF}}^4, \quad (3)$$

where F_{TOT} is the integrated flux above the Earth’s atmosphere and θ is the limb-darkened angular diameter. The challenge in calculating T_{EFF} is not the observation; rather, it is accounting for the flux emitted at wavelengths not readily observable from the ground, setting the zero points for converting magnitudes to fluxes and correcting the observed photometry for interstellar and atmospheric extinction.

To integrate the flux over the wavelength range from 0.36 μm to 10 μm , we used Johnson 11 color photometry (Johnson et al. 1966). For shorter wavelengths, OAO-2 data were used (Code et al. 1980). The IRAS point source catalog was used to extend the data to longer wavelengths, but in no case was there significant flux at these wavelengths. For wavelengths longer than 400 nm, we interpolated between broadband fluxes using a best fit Planck function. For shorter wavelengths where this is not a good approximation to the shape of the spectrum, a piecewise linear interpolation was used instead. For consistency we used this procedure for all stars even though higher resolution spectrophotometry is available for some of these stars. A comparison of that photometry to our integrations revealed a maximum discrepancy of 4 percent. The zero points for our flux scale were set by averaging the Vega calibrations from Hayes and Latham (1975) and Tug et al. (1977) for the visible and using the values from Cohen et al. (1992) for the infrared.

The most uncertain part of the procedure is correcting for interstellar extinction. Methods based on using the color of the star seem a little circular since we plan to use the scatter in the relationship between T_{EFF} and color as a measure of the quality of the results. A more serious problem with these methods is they cannot differentiate between circumstellar and interstellar extinction. An effective temperature calculation needs an integrated flux corrected for interstellar extinction but not for circumstellar absorption since the energy absorbed by circumstellar material will be properly included in the integrated flux when it is reradiated in the thermal infrared.

As a result, we based our values of V-band extinction, A_V , on Arenou et al. (1992). They binned their stars in galactic coordinates then used magnitudes and spectroscopic parallaxes to estimate extinction as a function of distance within each bin. We used those functions to determine the extinction of our program stars. The major disadvantage of this method is the coarseness of the grid used to determine the function. Advantages include separation of interstellar from circumstellar extinction, an independence of the extinction measurement from properties of the star and an intrinsic estimate of its accuracy. The V-band extinction uncertainty ranges from about 0.15 magnitudes for the stars with the lowest extinction to as much as 50% for the highest extinction stars. We decreased the calculated values of A_V by 10% since Arenou et al. (1992) used an unusually large values for $R_V = A_V/E(B - V)$.

Because interstellar extinction corrections cannot be made with an uncertainty smaller than a few tenths of a magnitude, performing these corrections on low extinction sources will decrease the precision of the flux measurements without improving their accuracy. Most of the stars we observed fall in this category. They are bright and close, and there is almost no extinction within 100 pc of the sun. We applied no extinction correction for stars within 100 pc of the sun and for

stars with an estimated $A_V < 0.2$ magnitudes. To the fifteen stars to which we applied corrections, the adopted values of A_V and their uncertainties are presented in Table 7.

The effective temperatures are presented in the last column of Table 4 and are shown as a function of $(V - K)$ in Figure 3. For the cool stars, the relationship between T_{EFF} and $(V - K)$ is tight. For warm stars, the supergiants are shown with systematically higher temperatures. Unfortunately, the four implicated supergiants (HR1017, HR1605, HR7796 and HR7924) all have large extinctions, and there are claims in the literature for significantly lower extinctions for three of these stars (Welty et al. 2001; Gray & Napier 2001). Moreover, if we assume the stars have zero extinction, the bifurcation of the relationship for the blue stars disappears. When we impose no extinction corrections, only HR8316 deviates significantly from a single function of T_{EFF} versus $(V - K)$. We will leave the determination of the reality of this bifurcation to others and use the extinction measurements as a flag; the stars listed in Table 7 are not included in the rest of the analysis of this section.

The simplest relationship we found that fits the data is

$$\log_{10}(T_{\text{EFF}}) = 3.972 - 0.176(V - K) + 0.024(V - K)^2 - 0.0013(V - K)^3 \quad (4)$$

The use of a higher order polynomial does not reduce the residuals, which are shown in Figure 4.

To estimate the precision with which we can measure effective temperatures, we restrict the discussion to the 43 luminosity class III stars. None of these stars has significant extinction. The standard deviation of the residuals for these stars is 51K. The χ^2_ν is 2.4 if we assume 2% flux errors, and reduces to 1 with reasonable 4.5% flux errors. Using all 62 stars of all luminosity classes, the standard deviation of the residuals increases to 89K and the χ^2_ν increases to 1.6 (using the 4.5% flux errors), but no luminosity class is systematically offset from Equation 4.

7. Stellar Surface Brightness

Following Hindsley&Bell (1989), we define the log of the stellar surface brightness as

$$S_V = m_V + 5\log(\theta), \quad (5)$$

where m_V is the apparent visual magnitude on the Johnson system and θ is the limb-darkened angular diameter in milliarcseconds. This definition follows the same convention as magnitudes, with a smaller value of S_V implying a brighter surface.

A plot of S_V versus $(V - R)$ is shown in Figure 5. Stars of all luminosity classes are included. Because this correlation is fairly tight, it can be used to predict θ . The lowest order polynomial fit to this relationship that does not show obvious systematics in the residuals is a cubic,

$$S_V = 2.661 + 4.178(V - R) + 0.047(V - R)^2 - 0.131(V - R)^3 \quad (6)$$

and is shown as the solid line in Figure 5. The residuals are shown in Figure 6.

The scatter in this relationship is larger than expected. Assuming the angular diameter errors from Table 2 and errors of 0.01 magnitudes in both V and $(V - R)$, $\chi^2_\nu = 22$. The χ^2_ν can be reduced to 1 by assuming the systematic errors in θ_{UD} are 6.5%, not the 1% estimated from the internal consistency arguments. Errors this large are ruled out by the consistency of these data with other published diameters. Alternatively, using the diameter errors from Table 2, photometric errors of 0.062 magnitudes in both V and $(V - R)$ are needed to explain the scatter.

To further investigate the nature of the excess scatter, we correlated S_V with another photometric index. A plot of S_V versus $(V - K)$ is shown in Figure 7 along with a fit to the data. The residuals are shown in Figure 8. This time a quadratic fit is sufficient:

$$S_V = 2.658 + 1.385(V - K) - 0.021(V - K)^2 \quad (7)$$

Once again, assuming 1% photometric errors and the diameter errors in Table 2, the scatter is larger than expected, with $\chi^2_\nu = 3.9$. We can reduce χ^2_ν to 1 by increasing the minimum angular diameter error to 2.6% or by increasing the assumed photometric error to 0.035 magnitudes. Photometric errors of this magnitude are not out of the question.

An argument that the scatter is not due to the angular diameter measurements can be made by comparing the residuals in Figures 5 and 7. If the scatter in these two relationships is due primarily to errors in the angular diameters, the residuals should be strongly correlated. Figure 9 compares the residuals. The formal correlation coefficient is 0.17, implying that the variance of the uncorrelated component of the noise is 4.8 times larger than the correlated component. Since the correlated noise is in part from θ and in part from m_V , while the uncorrelated noise is from $(V - R)$ or $(V - K)$, it is difficult to understand how this correlation coefficient is consistent with increasing the uncertainty in θ to explain the large χ^2_ν in Equations 6 and 7.

The remaining obvious source of observational noise in the surface brightness relationships that needs to be addressed is interstellar extinction. For the accuracy of S_V to be limited by the accuracy of the diameters, the V band extinction, A_V , must be determined to about 1%. This is at least a factor of 10 better than what can currently be accomplished. Fortunately, interstellar extinction also changes the color of the star. Using values of the interstellar extinction presented by Cardelli et al. (1989) for $R_V = 3.1$, we find the reddening curve runs almost parallel to the surface brightness curve in Figure 5. The reddening curve has a slope of 4.0, matching the slope of the surface brightness curve at $(V - R) = 0.8$. Therefore, interstellar extinction should not increase the scatter unless R_V has a significantly anomalous value.

We conclude that the scatter is not due to the measurements but is intrinsic to the surface brightness relationships.

8. The Wavelength Dependence of Uniform-Disk Diameters

8.1. Comparison Among Visual Diameters

Because stellar limb darkening varies with wavelength, a star’s equivalent uniform-disk angular diameter should also vary with wavelength. Ridgway et al. (1982) present an early measurement of this effect. The ratio of uniform-disk angular diameter at 800 nm to 550 nm is shown in Figure 10, and the ratio of 800 nm to 451 nm uniform-disk diameters is shown in Figure 11. The solid lines are predictions from model atmospheres and represent luminosity classes I, III and V.

The observed ratios are slightly larger than predicted. This is equivalent to saying the observed increase in limb darkening toward shorter wavelengths is larger than predicted by the model atmospheres. The ratio of observed 800 nm to 550 nm angular diameters averages 0.8% too large, while the ratio of 800 nm to 451 nm angular diameters averages 1.9% larger than predicted by the models. These deviations from the models are, however, only marginally significant. Comparing the data directly to the models results in χ^2_ν values of 0.74 for the 800 nm/550 nm ratio and 2.2 for the 800 nm/451 nm ratio. If we increase the limb darkening of the models at the shorter wavelengths by the values given above, the χ^2_ν are reduced to 0.58 and 1.9 respectively.

Since there are still very few direct measurements of stellar limb darkening, we summarize these data as an aid to anyone interested in understanding this variation. We calculated S_V using uniform-disk diameters. These values are not strictly surface brightnesses. They all refer to the same V magnitude, and since the physical size of the stars should not depend on wavelength, neither should S_V . The best linear and quadratic fits to these quantities as a function of photometric color are

$$S_V(800 \text{ nm}) = 2.767 + 1.23(V - K) \quad (8)$$

$$S_V(550 \text{ nm}) = 2.663 + 1.24(V - K) \quad (9)$$

$$S_V(500 \text{ nm}) = 2.554 + 1.28(V - K) \quad (10)$$

$$S_V(451 \text{ nm}) = 2.549 + 1.27(V - K) \quad (11)$$

$$(12)$$

and

$$S_V(800 \text{ nm}) = 2.607 + 1.346(V - K) - 0.0180(V - K)^2 \quad (13)$$

$$S_V(550 \text{ nm}) = 2.634 + 1.266(V - K) - 0.0036(V - K)^2 \quad (14)$$

$$S_V(500 \text{ nm}) = 2.691 + 1.202(V - K) + 0.0107(V - K)^2 \quad (15)$$

$$S_V(451 \text{ nm}) = 2.496 + 1.330(V - K) - 0.0140(V - K)^2 \quad (16)$$

The correlation of these S_V s and photometric color is as tight as when limb-darkened diameters are used and provide uniform-disk diameters with an accuracy of about 3% over the range $0 < (V - K) < 6$.

8.2. Comparison Between Visual and Infrared Diameters

Because of both the increasing number of measured infrared angular diameters and the increasing number of operational infrared interferometers, it is important to compare the visible and infrared measurements. Figure 12 shows the ratio of K band uniform-disk diameters from the literature to Mark III 800 nm uniform-disk diameters. The I2T data were taken from Di Benedetto&Rabbia (1987), Di Benedetto&Ferluga (1990) and Di Benedetto&Foy (1986), the IOTA data were taken from Dyck et al. (1996) and the PTI data from van Belle et al. (1999a). Once again, the three solid lines show the expected relationship for different luminosity classes derived from Kurucz models. There is an obvious trend in these data. Stars with $(V - K)$ colors between 2 and 4 are in good agreement with the models. However for cooler stars, the ratios of infrared to visible diameters are smaller than expected. This trend appears to be significant, but its interpretation is complicated by the inhomogeneous nature of the data. For example, Dyck et al. (1996) pointed out that for the stars observed both with IOTA and with I2T, the IOTA diameters are systematically smaller for the large stars and systematically larger for the small stars. Using a single data set should help untangle variations with color from variation between instruments.

The largest high-quality, homogeneous set of infrared diameters is from the Palomar Testbed Interferometer, PTI (van Belle et al. 1999a). Unfortunately the only stars in common between the PTI and the Mark III are five of the warmest stars in Figure 12. Both interferometers observed both warmer and cooler stars; to extend this comparison, an indirect approach is needed. This comparison can be made through surface brightness relationships.

We start by calculating S_V for the stars observed by PTI using the PTI uniform-disk diameters. These are shown as a function of $(V - K)$ in Figure 13. Two obvious outliers (HR274 and HR7759) were not included in the analysis. The five stars also observed by the Mark III are shown with solid symbols. Note that they all fall along the lower edge of the distribution. The solid line shows the value we would expect using 800 nm data and Equation 13. There is an obvious systematic trend in this data, with the $2.2 \mu\text{m}$ data falling systematically below the 800 nm relationship for the cooler stars and above the relationship for the warmer stars. Linear and quadratic fits through the PTI data give the following relationships

$$S_V(2.2\mu\text{m}) = 3.197 + 1.126(V - K) \quad (17)$$

$$S_V(2.2\mu\text{m}) = 3.426 + 1.002(V - K) + 0.015(V - K)^2 \quad (18)$$

For each of the PTI stars, Equation 13 was used to predict the uniform-disk diameter that star would have at 800 nm. The ratio of the $2.2 \mu\text{m}$ PTI diameter to the 800 nm prediction is shown in Figure 14. Again, the stars observed by both the PTI and the Mark III are shown with filled symbols.

For stars cooler than $(V - K) = 4$, this ratio is smaller than the expectation from stellar atmosphere models, with the discrepancy increasing for larger values of $(V - K)$. The discrepancy

appears significant and is consistent with the trend in Figure 12. A smaller value of S_V implies a higher surface brightness which in turn implies either a smaller stellar diameter or more limb darkening. If it is the latter, it contradicts the standard argument that infrared diameters should be used to determine effective temperatures because the limb darkening is smaller at those wavelengths. It seems more likely that these trends are due to the former cause, i.e., differences between the diameters in the two wavelength regimes. Such differences are inconsistent with the standard stellar models but can probably be explained by invoking more extended stellar atmospheres. An extended atmosphere would enlarge the 800 nm diameters more than the K band diameters, since both the continuum and molecular line opacities are larger at the shorter wavelength. In particular, our 800 nm bandpass is contaminated with TiO. Some evidence supporting this view can be found in Quirrenbach et al. (1993). They presented uniform-disk diameters in TiO bands that are significantly larger than the adjacent continuum for similar stars.

For the 19 stars with $2 < (V - K) < 3$ (spectral types G8 to K2), the mean uniform-disk diameter ratio is 1.12 (median of 1.10), larger than the predicted ratio, which lies between 1.03 and 1.04. The five stars in common with the the Mark III observations fall in this color range but their diameter ratios ranges from 1.0 to 1.085 with a mean of 1.03. These values, which are in good agreement with the models, fall in the lower half of the distribution for the PTI stars. We know there is intrinsic noise in the surface brightness relationship, so this disagreement, though surprising, may not be significant.

There remain the four PTI stars with $(V - K) < 2.0$. Although the error bars are large, these stars have infrared diameters from 20% to 40% larger than the predicted 800 nm diameter. Stellar atmosphere models predict that the uniform disk diameters should be only 3% larger at $2.2 \mu\text{m}$. For α Lyr, Equation 13 predicts an 800 nm uniform-disk diameter of 3.2 mas, in agreement with the measured angular diameter. Equation 17, fit to the PTI data gives an angular diameter of 4.3 mas. van Belle (1999b) noticed this discrepancy but attributed it to the variation of angular diameter with luminosity class, giving equations for limb-darkened diameters consistent with the Mark III data for main sequence stars and with the PTI data for evolved stars. This explanation is not the complete answer since the stars observed with the Mark III in this temperature range consist of main sequence, giant, and supergiant stars and they are all consistent with the same surface brightness relationship. We leave this discrepancy unexplained.

9. Summary

In addition to their application to determining effective temperatures, accurately estimated angular diameters are needed for calibration of optical interferometry data. As we push to longer baselines, it is becoming increasingly difficult to find stars that are small enough to appear unresolved. Unless we find a way to transfer the calibration from short to long baselines, the quality of optical interferometric data will remain limited by our ability to calibrate.

It has long been customary to fit a uniform disk model to the visibility data, then convert the uniform disk diameter to a limb darkened value using a correction factor. This technique is used because it cleanly separates the data, represented by the uniform disk diameter, from the details of the stellar models needed to correct for the limb darkening. By convention, the conversion factor is the ratio of the diameter of the limb-darkened to the uniform-disk model when the models are forced to agree at $V^2 = 0.3$ (Hanbury Brown et al. 1974). This conversion varies by a few parts in a thousand depending upon how the models are forced to agree. As the accuracy of interferometrically determined angular diameters surpasses the 1% level, this method will no longer work, and it will be necessary to fit the data directly to limb darkened models.

In this paper, we have presented measured angular diameters for 85 stars, more than half with formal errors less than 1%. Although it is good to claim high accuracy based on internal consistency arguments, it is better to confirm that accuracy based on consistency with other results. Although several interferometers are producing stellar angular diameters, most of the observations are at different wavelengths or of different stars. With that caveat, the comparison of our results with other published diameters at similar wavelengths is satisfactory.

The comparison of our results with published infrared diameters is somewhat more problematic. The PTI in particular has produced a large number of diameter measurements, but there are only five stars in common between our list and theirs. For these five, the ratios of infrared to visual uniform disk diameters are in good agreement with stellar atmosphere models. However, these five cover only a small range of effective temperatures.

To make a broader comparison, an indirect approach using surface brightness relationships is the best we can do, although it is not optimum. We find that the ratio of 2.2 μm PTI uniform disk diameters to the Mark III 800 nm uniform disk diameters is smaller than the ratio predicted by the models for cool stars, and larger for warm stars. The discrepancy for cool stars could be telling us something interesting about the physical conditions in their outer atmospheres. It is difficult to understand the discrepancy for warm stars.

This work was funded by the Office of Naval Research and the Oceanographer of the Navy. This work made use of the SIMBAD literature database, operated at CDS, Strasbourg, France. The observations upon which the paper is based absorbed hundreds of hours of observing time which would not have been possible without the dedicated support of the interferometer operators, Craig Denison and Lu Rarogiewicz. We also thank Mike Shao and Mark Colavita for the initial construction of the Mark III and Roger Bell, Ben Taylor and Paolo Di Benedetto for useful discussions. Finally, we would be negligent by not acknowledging the thorough comments of a reviewer who left his mark on this paper with a number of thought- and work- provoking comments.

Table 1. Observations

HR	Total Days	Total Number of Scars at Baseline Length (meters)																		
		3.0	4.3	5.3	6.6	6.9	7.5	8.2	11.4	15.2	15.4	19.1	19.4	19.7	23.1	23.3	23.6	27.0	27.6	29.1
165	6	5	18	13	3
168	13	12	36	8	...	8	...	26	18	29	...	15
337	11	16	19	9	...	8	...	23	29
603	11	14	23	8	...	8	...	27	10	24	...	20
617	16	15	19	9	...	8	...	27	24	22	...	42	23
643	9	...	16	7	8	5	6	...	9	...	9
834	6	10	4	7	...	9
843	8	6	7	5	6	...	8	...	11
911	3	8	...	7	...	4
921	3	...	16	12
1017	6	...	2	14	...	5	7	...	9	...	7
1231	4	...	10	4	5	3
1373	12	15	11	39	4	...	15	15	23	4	17	17
1409	9	7	5
1457	8	12	5	8	...	13	...	12
1577	7	...	12	9	...	2	18	2	...	14
1601	9	...	14	10	1	...	1	...	8	15
1605	6	4	2	9
2091	12	...	15	5	28	29	7
2216	10	3	15	3	35
2286	7	...	9	8	3	20
2473	7	...	8	4	19	4	...	2
2491	6	...	5	3	7	...	4	10
2943	11	11	...	10	...	10	5	11	...	14	...	17	...
2990	17	12	17	8	...	13	...	7	9	6	...	16	...	1
3249	6	...	4	3	6	3	6
3547	5	...	3	2	6	8
3705	9	...	14	2	18	5	7	4
3748	6	...	12	5	...	10	...	7
3873	8	2	8	4	8	3
4069	12	4	22	1	4	18	7	10
4301	7	12	7
4335	1
4377	7	11	7	15	7
4434	6	...	12	10	11	4
4517	4	...	7	1	6

Table 1—Continued

HR	Total Days	Total Number of Scans at Baseline Length (meters)														23.3	23.6	27.0	27.6	29.1	3
		3.0	4.3	5.3	6.6	6.9	7.5	8.2	11.4	15.2	15.4	19.1	19.4	19.7	23.1						
4910	3	3	...	11	
4932	11	11	9	...	12	12	...	2	2	
5235	24	4	4	3	...	3	23	...	13	26	...	21	33	...	1	
5340	7	14	21	6	...	1	
5563	13	4	3	3	6	3	20	10	
5589	7	2	8	1	5	
5602	5	14	...	8	
5681	12	13	12	...	9	14	11	6	
5854	10	7	...	11	13	23	...	9	
6056	9	2	4	1	...	4	5	...	10	4	
6132	8	3	9	12	...	11	
6134	2	5	7	
6146	6	5	22	4	...	5	
6148	31	5	22	11	...	5	36	...	11	21	...	23	66	23	13	11	
6212	14	4	11	9	...	13	13	8	10	
6220	1	9	
6406	5	3	6	
6418	11	5	5	2	...	5	12	7	2	
6536	12	5	12	11	13	9	...	3	
6623	14	9	5	...	12	8	7	12	
6695	13	4	10	...	17	5	...	5	...	5	
6705	8	1	7	4	10	11	
7001	16	1	11	13	...	21	...	1	5	...	6	...	4	
7139	6	...	9	4	12	
7157	11	1	21	7	...	7	...	11	
7310	5	6	13	...	3	
7405	13	14	19	...	4	...	9	6	
7417	9	...	7	8	...	5	...	4	...	10	8	
7525	23	2	9	8	...	10	3	5	17	3	23	...	5	...	10	
7536	13	...	7	...	11	7	4	11	12	...	14	
7557	36	4	11	7	...	10	...	15	12	...	24	...	14	...	9	23	10	1	
7635	20	2	10	11	...	12	...	5	4	3	23	...	5	...	11	
7735	6	10	
7751	17	2	6	6	...	13	16	7	11	...	13	...	14	
7796	20	1	11	6	1	9	18	...	21	...	1	
7924	25	3	9	10	...	12	...	7	21	10	13	1	12	...	10	

Table 1—Continued

HR	Total Days	Total Number of Scans at Baseline Length (meters)															23.3	23.6	27.0	27.6	29.1	3
		3.0	4.3	5.3	6.6	6.9	7.5	8.2	11.4	15.2	15.4	19.1	19.4	19.7	23.1							
7949	14	...	13	7	1	8	7	8	...	8	17
8079	27	2	8	9	...	9	...	34	25	37	33	32	8	...	49	7
8115	17	9	...	8	11	10	18	...	2	6	11
8225	9	12	28	...	9	...	14
8308	12	3	8	11	...	11	...	3	1
8316	9	2	19	7	7
8414	4	...	9	5	5
8465	10	2	6	8	...	6	...	6	...	9	8	12
8667	14	1	...	3	...	7	4	5	...	12
8684	15	2	...	4	9	4	4	...	9
8698	10	...	11	5	6	...	8	...	9	...	2
8775	15	14	10	10	...	16	...	32
8796	10	...	11	8	14	...	9	...	20	13

Table 2. Angular Diameter Measurements

HR	Name	Uniform Disk Angular Diameters (mas)				Limb Darkened Diameter (mas)
		800 nm	550 nm	500 nm	451 nm	
165	δ And	3.874 ± 0.039	3.643 ± 0.182	3.663 ± 0.051	3.624 ± 0.072	4.136 ± 0.041
168	α Cas	5.284 ± 0.053	5.113 ± 0.072	5.116 ± 0.212	4.890 ± 0.098	5.608 ± 0.056
337	β And	12.782 ± 0.128	12.450 ± 0.297	12.199 ± 0.171	11.814 ± 0.293	13.749 ± 0.137
603	γ_1 And	7.326 ± 0.073	7.110 ± 0.100	6.897 ± 0.097	6.535 ± 0.131	7.814 ± 0.078
617	α Ari	6.407 ± 0.064	6.153 ± 0.086	6.263 ± 0.120	5.795 ± 0.116	6.827 ± 0.068
643	60 And	2.824 ± 0.047	2.599 ± 0.060	2.907 ± 0.048
834	η Per	4.977 ± 0.051	4.780 ± 0.083	5.381 ± 0.055
843	17 Per	3.777 ± 0.038	3.572 ± 0.087	4.056 ± 0.041
911	α Cet	12.269 ± 0.237	...	11.473 ± 0.251	11.325 ± 0.410	13.238 ± 0.256
921	ρ Per	15.085 ± 0.151	15.355 ± 0.229	16.555 ± 0.166
1017	α Per	3.055 ± 0.034	2.986 ± 0.042	...	2.793 ± 0.056	3.188 ± 0.035
1231	γ Eri	8.668 ± 0.161	8.361 ± 0.139	9.332 ± 0.173
1373	δ_1 Tau	2.207 ± 0.031	2.143 ± 0.031	...	2.120 ± 0.068	2.338 ± 0.033
1409	ϵ Tau	2.522 ± 0.030	2.422 ± 0.034	...	2.275 ± 0.103	2.671 ± 0.032
1457	α Tau	19.626 ± 0.196	20.044 ± 0.670	19.491 ± 0.290	19.006 ± 0.380	21.099 ± 0.211
1577	ι Aur	7.004 ± 0.070	6.786 ± 0.095	...	6.786 ± 0.337	7.500 ± 0.075
1601	π_6 Ori	2.598 ± 0.052	2.472 ± 0.055	2.781 ± 0.056
1605	ϵ Aur	2.006 ± 0.082	...	1.946 ± 0.058	2.094 ± 0.042	2.096 ± 0.086
2091	π Aur	8.735 ± 0.087	8.417 ± 0.138	9.558 ± 0.096
2216	η Gem	10.914 ± 0.109	11.426 ± 0.551	11.789 ± 0.118
2286	μ Gem	13.989 ± 0.140	13.483 ± 0.189	15.118 ± 0.151
2473	ϵ Gem	4.406 ± 0.044	4.467 ± 0.115	...	4.256 ± 0.151	4.703 ± 0.047
2491	α CMa	5.823 ± 0.105	5.421 ± 0.255	5.993 ± 0.108
2943	α CMi	5.228 ± 0.052	5.323 ± 0.075	...	5.302 ± 0.106	5.446 ± 0.054
2990	β Gem	7.529 ± 0.075	7.255 ± 0.102	7.414 ± 0.113	7.131 ± 0.143	7.980 ± 0.080
3249	β Cnc	4.885 ± 0.064	4.797 ± 0.084	5.238 ± 0.069
3576	ρ UMa	5.222 ± 0.134	5.640 ± 0.145
3705	α Lyn	7.012 ± 0.070	6.751 ± 0.095	7.538 ± 0.075
3748	α Hya	9.088 ± 0.091	8.740 ± 0.122	9.727 ± 0.097
3873	ϵ Leo	2.446 ± 0.074	2.446 ± 0.067	...	2.429 ± 0.121	2.575 ± 0.078
4069	μ UMa	7.924 ± 0.079	7.579 ± 0.106	...	6.726 ± 0.296	8.538 ± 0.085
4301	α UMa	6.337 ± 0.093	6.117 ± 0.128	...	6.680 ± 0.134	6.739 ± 0.099
4335	ψ UMa	3.866 ± 0.039	3.708 ± 0.061	4.120 ± 0.041
4377	ν UMa	4.442 ± 0.044	4.272 ± 0.060	...	3.960 ± 0.193	4.759 ± 0.048
4434	λ Dra	5.963 ± 0.064	5.645 ± 0.119	6.430 ± 0.069
4517	ν Vir	5.681 ± 0.107	5.394 ± 0.087	6.116 ± 0.115
4910	δ Vir	9.911 ± 0.099	9.483 ± 0.133	10.709 ± 0.107

Table 2—Continued

HR	Name	Uniform Disk Angular Diameters (mas)				Limb Darkened Diameter (mas)
		800 nm	550 nm	500 nm	451 nm	
4932	ϵ Vir	3.115 \pm 0.031	3.001 \pm 0.042	...	2.934 \pm 0.102	3.283 \pm 0.033
5235	η Boo	2.176 \pm 0.024	2.126 \pm 0.030	...	2.113 \pm 0.042	2.269 \pm 0.025
5340	α Boo	19.995 \pm 0.231	19.473 \pm 0.273	18.848 \pm 0.264	18.927 \pm 0.463	21.373 \pm 0.247
5563	β UMi	9.608 \pm 0.096	9.226 \pm 0.129	...	8.842 \pm 0.185	10.301 \pm 0.103
5589	R UMi	9.780 \pm 0.157	10.588 \pm 0.170
5602	β Boo	2.350 \pm 0.062	2.286 \pm 0.032	...	2.069 \pm 0.097	2.477 \pm 0.065
5681	δ Boo	2.609 \pm 0.028	2.538 \pm 0.036	...	2.486 \pm 0.110	2.764 \pm 0.030
5854	α Ser	4.557 \pm 0.046	4.395 \pm 0.062	...	4.295 \pm 0.101	4.846 \pm 0.048
6056	δ Oph	9.714 \pm 0.109	9.255 \pm 0.130	...	8.664 \pm 0.374	10.471 \pm 0.117
6132	η Dra	3.535 \pm 0.067	3.398 \pm 0.058	...	3.333 \pm 0.080	3.722 \pm 0.071
6134	α Sco	38.727 \pm 0.389	39.852 \pm 0.558	39.759 \pm 0.399
6146	30 Her	17.540 \pm 0.175	21.084 \pm 0.543	21.612 \pm 0.859	...	19.086 \pm 0.191
6148	β Her	3.285 \pm 0.033	3.204 \pm 0.045	...	3.086 \pm 0.062	3.462 \pm 0.035
6212	ζ Her	2.261 \pm 0.049	2.133 \pm 0.030	...	1.989 \pm 0.049	2.367 \pm 0.051
6220	η Her	2.488 \pm 0.032	2.344 \pm 0.051	2.624 \pm 0.034
6406	α_1 Her	35.091 \pm 0.428	36.829 \pm 0.560	36.026 \pm 0.439
6418	π Her	4.942 \pm 0.063	4.747 \pm 0.066	5.275 \pm 0.067
6536	β Dra	3.059 \pm 0.050	2.995 \pm 0.057	...	2.949 \pm 0.096	3.225 \pm 0.053
6623	μ Her	1.863 \pm 0.037	1.808 \pm 0.025	...	1.609 \pm 0.076	1.953 \pm 0.039
6695	θ Her	2.976 \pm 0.030	2.895 \pm 0.041	3.170 \pm 0.032
6705	γ Dra	9.193 \pm 0.119	8.813 \pm 0.259	9.860 \pm 0.128
7001	α Lyr	3.149 \pm 0.031	2.996 \pm 0.047	...	2.975 \pm 0.059	3.225 \pm 0.032
7139	δ_2 Lyr	10.512 \pm 0.142	11.530 \pm 0.156
7157	13 Lyr	16.614 \pm 0.207	18.005 \pm 0.252	18.016 \pm 0.224
7310	δ Dra	3.075 \pm 0.050	2.978 \pm 0.042	...	2.821 \pm 0.097	3.254 \pm 0.053
7405	α Vul	4.151 \pm 0.042	3.976 \pm 0.078	4.458 \pm 0.045
7417	β_1 Cyg	4.543 \pm 0.045	4.470 \pm 0.063	4.834 \pm 0.048
7525	γ Aql	6.788 \pm 0.068	6.536 \pm 0.092	...	6.488 \pm 0.206	7.271 \pm 0.073
7536	δ Sge	8.426 \pm 0.110	8.526 \pm 0.271	9.151 \pm 0.119
7557	α Aql	3.348 \pm 0.033	3.263 \pm 0.046	...	3.115 \pm 0.062	3.462 \pm 0.035
7635	γ Sge	5.799 \pm 0.058	5.509 \pm 0.077	6.225 \pm 0.062
7735	31 Cyg	4.086 \pm 0.041	3.811 \pm 0.079	4.362 \pm 0.044
7751	32 Cyg	5.022 \pm 0.050	4.766 \pm 0.067	5.423 \pm 0.054
7796	γ Cyg	2.891 \pm 0.029	2.811 \pm 0.039	...	2.749 \pm 0.055	3.017 \pm 0.030
7924	α Cyg	2.337 \pm 0.058	2.256 \pm 0.057	...	2.246 \pm 0.052	2.420 \pm 0.060
7949	ϵ Cyg	4.354 \pm 0.044	4.274 \pm 0.060	4.157 \pm 0.058	4.084 \pm 0.082	4.612 \pm 0.046
8079	ξ Cyg	5.359 \pm 0.054	5.121 \pm 0.072	5.787 \pm 0.058

Table 2—Continued

HR	Name	Uniform Disk Angular Diameters (mas)				Limb Darkened Diameter (mas)
		800 nm	550 nm	500 nm	451 nm	
8115	ζ Cyg	2.666 ± 0.027	2.613 ± 0.037	...	2.546 ± 0.060	2.821 ± 0.028
8225	2 Peg	4.201 ± 0.044	4.085 ± 0.079	4.521 ± 0.047
8308	ϵ Peg	6.967 ± 0.234	6.723 ± 0.295	7.459 ± 0.251
8316	μ Cep	18.672 ± 0.435	20.584 ± 0.480
8414	α Aqr	3.073 ± 0.054	2.967 ± 0.042	...	2.793 ± 0.135	3.237 ± 0.057
8465	ζ Cep	4.885 ± 0.049	4.746 ± 0.066	5.234 ± 0.052
8667	λ Peg	2.251 ± 0.045	2.155 ± 0.041	2.387 ± 0.048
8684	μ Peg	2.366 ± 0.038	2.333 ± 0.042	2.496 ± 0.040
8698	λ Aqr	7.582 ± 0.097	7.339 ± 0.105	8.186 ± 0.105
8775	β Peg	16.528 ± 0.165	16.326 ± 0.229	16.464 ± 0.230	15.970 ± 0.319	17.982 ± 0.180
8796	56 Peg	2.190 ± 0.048	2.031 ± 0.060	2.338 ± 0.051

Table 3. Zero-Spacing Visibility Amplitude

Star		800 nm	Zero Spacing Visibility Amplitudes		
			550 nm	500 nm	451 nm
165	δ And	0.993 ± 0.006	1.000	1.000	0.987 ± 0.025
168	α Cas	0.991 ± 0.002	0.975 ± 0.012	0.975 ± 0.007	0.972 ± 0.007
337	β And	1.003 ± 0.002	1.000	0.994 ± 0.010	0.985 ± 0.022
603	γ_1 And	0.983 ± 0.002	1.000	0.880 ± 0.004	0.780 ± 0.006
		0.97		0.88	0.61
617	α Ari	1.001 ± 0.002	1.000	1.000 ± 0.006	0.978 ± 0.007
643	60 And	0.991 ± 0.005	1.006 ± 0.011
834	η Per	0.979 ± 0.006	0.981 ± 0.015
843	17 Per	1.005 ± 0.004	1.012 ± 0.017
911	α Cet	1.000 ± 0.007	...	0.984 ± 0.016	0.964 ± 0.029
921	ρ Per	1.000 ± 0.006	1.000
1017	α Per	0.996 ± 0.004	0.993 ± 0.007	...	0.950 ± 0.012
1231	γ Eri	0.992 ± 0.008	0.986 ± 0.015
1373	δ_1 Tau	1.007 ± 0.003	1.002 ± 0.006	...	1.036 ± 0.021
1409	ϵ Tau	1.002 ± 0.005	0.999 ± 0.008	...	1.000
1457	α Tau	0.982 ± 0.005	1.000	1.000	1.000
1577	ι Aur	1.009 ± 0.004	1.019 ± 0.011	...	1.000
1601	π_6 Ori	1.005 ± 0.005	0.997 ± 0.012
1605	ϵ Aur	0.988 ± 0.012	...	0.983 ± 0.020	1.000
		1.00		1.00	
2091	π Aur	0.979 ± 0.005	0.946 ± 0.013
2216	η Gem	0.959 ± 0.006	0.939 ± 0.026
			0.92		
2286	μ Gem	1.009 ± 0.006	1.000
2473	ϵ Gem	0.987 ± 0.004	1.004 ± 0.014	...	1.000
2491	α CMa	0.976 ± 0.007	0.924 ± 0.026
		1.00			1.00
2943	α CMi	0.998 ± 0.003	1.000	...	1.001 ± 0.007
		1.00			1.00
2990	β Gem	1.006 ± 0.002	1.002 ± 0.007	1.011 ± 0.007	1.004 ± 0.007
3249	β Cnc	1.006 ± 0.006	1.028 ± 0.015
		1.00	1.00		

Table 3—Continued

		Zero Spacing Visibility Amplitudes			
Star		800 nm	550 nm	500 nm	451 nm
3576	ρ UMa	0.987 ± 0.012
3705	α Lyn	0.996 ± 0.004	1.002 ± 0.008
3748	α Hya	0.994 ± 0.005	0.997 ± 0.008
3873	ϵ Leo	0.997 ± 0.006	0.988 ± 0.010	...	1.002 ± 0.024
4069	μ UMa	1.001 ± 0.004	1.001 ± 0.007	...	0.977 ± 0.036
4301	α UMa	0.955 ± 0.010	0.901 ± 0.021	...	1.000
			0.93		
4335	ψ UMa	1.000	1.000
4377	ν UMa	1.007 ± 0.005	1.005 ± 0.012	...	1.000
4434	λ Dra	0.997 ± 0.005	1.017 ± 0.011
4517	ν Vir	0.990 ± 0.008	1.003 ± 0.014
4910	δ Vir	1.000	1.000
4932	ϵ Vir	1.006 ± 0.004	1.014 ± 0.007	...	1.041 ± 0.023
5235	η Boo	1.011 ± 0.002	1.021 ± 0.003	...	1.030 ± 0.007
			0.99		1.00
5340	α Boo	0.994 ± 0.008	1.000	1.000	1.000
			0.95		
5563	β UMi	1.004 ± 0.005	0.996 ± 0.009	...	1.006 ± 0.020
5589	R UMi	0.998 ± 0.006
		1.00			
5602	β Boo	1.004 ± 0.009	1.000	...	1.000
5681	δ Boo	1.004 ± 0.004	1.015 ± 0.006	...	1.045 ± 0.026
5854	α Ser	1.019 ± 0.004	1.033 ± 0.006	...	1.054 ± 0.016
6056	δ Oph	1.017 ± 0.006	1.015 ± 0.011	...	1.014 ± 0.035
6132	η Dra	1.008 ± 0.006	1.019 ± 0.011	...	1.050 ± 0.019
6134	α Sco	1.000	1.000
6146	30 Her	0.953 ± 0.006	1.000	1.000	...
6148	β Her	0.995 ± 0.002	0.995 ± 0.003	...	0.985 ± 0.006
			0.99		
6212	ζ Her	0.934 ± 0.005	0.950 ± 0.005	...	0.948 ± 0.012
			0.93		
6220	η Her	1.000	1.000

Table 3—Continued

		Zero Spacing Visibility Amplitudes			
Star		800 nm	550 nm	500 nm	451 nm
6406	α_1 Her	1.000	1.000
6418	π Her	1.004 \pm 0.004	1.002 \pm 0.007
6536	β Dra	0.980 \pm 0.004	0.961 \pm 0.009	...	0.961 \pm 0.018
6623	μ Her	0.997 \pm 0.004	1.010 \pm 0.006	...	0.995 \pm 0.016
6695	θ Her	1.005 \pm 0.004	1.015 \pm 0.007
6705	γ Dra	0.953 \pm 0.009	0.918 \pm 0.020
7001	α Lyr	1.007 \pm 0.003	1.000 \pm 0.008	...	1.009 \pm 0.008
7139	δ_2 Lyr	0.984 \pm 0.010
7157	13 Lyr	0.970 \pm 0.009	1.000
7310	δ Dra	1.000	1.000	...	1.000
7405	α Vul	1.005 \pm 0.004	1.006 \pm 0.016
7417	β_1 Cyg	0.931 \pm 0.004	0.822 \pm 0.009
			0.86		
7525	γ Aql	1.008 \pm 0.003	1.006 \pm 0.005	...	1.006 \pm 0.018
7536	δ Sge	1.001 \pm 0.007	0.983 \pm 0.026
		0.98	0.92		
7557	α Aql	1.003 \pm 0.002	1.000 \pm 0.004	...	1.002 \pm 0.006
7635	γ Sge	1.003 \pm 0.003	0.999 \pm 0.004
7735	31 Cyg	0.983 \pm 0.005	0.849 \pm 0.016
			0.94		
7751	32 Cyg	0.990 \pm 0.003	0.947 \pm 0.008
			0.99		
7796	γ Cyg	0.999 \pm 0.003	0.998 \pm 0.007	...	0.987 \pm 0.011
7924	α Cyg	1.001 \pm 0.003	0.996 \pm 0.005	...	0.993 \pm 0.006
7948	γ_2 Del	...	1.000
7949	ϵ Cyg	0.999 \pm 0.003	1.008 \pm 0.006	1.000	1.002 \pm 0.017
8079	ξ Cyg	0.997 \pm 0.002	0.992 \pm 0.004
8115	ζ Cyg	1.000 \pm 0.003	1.001 \pm 0.005	...	0.995 \pm 0.018
		1.00	1.00		1.00
8225	2 Peg	0.993 \pm 0.005	0.997 \pm 0.017
8308	ϵ Peg	0.998 \pm 0.005	0.988 \pm 0.012
8316	μ Cep	0.806 \pm 0.012

Table 3—Continued

			Zero Spacing Visibility Amplitudes			
Star			800 nm	550 nm	500 nm	451 nm
8414	α	Aqr	1.007 \pm 0.006	1.018 \pm 0.012	...	1.000
8465	ζ	Cep	0.991 \pm 0.003	0.995 \pm 0.005
8667	λ	Peg	1.009 \pm 0.006	1.024 \pm 0.010
8684	μ	Peg	1.004 \pm 0.004	1.002 \pm 0.007
8698	λ	Aqr	0.993 \pm 0.007	0.977 \pm 0.013
8775	β	Peg	0.999 \pm 0.004	1.000	1.000	1.000
8796	56	Peg	1.001 \pm 0.005	0.987 \pm 0.012

Note. — If an entry for a star does not have an error estimate, that value was assumed in the diameter fit. Ellipses indicate no fit was performed. This data set contains a number of wide binary star systems whose zero spacing visibility amplitude should not be 1. Each of these stars has a second line in its entry where an estimate of V_0 has been given. This estimate is based on published knowledge of the companion.

Table 4. Photometric Data

HR	Name	V	$(V - R)$	$(V - K)$	Flux (nW/m ²)	Spectral Type	$T_{\text{EFF}}(K)$
165	δ And	3.28	0.92	2.80	2.12	K3.0 III	4392 \pm 54
168	α Cas	2.23	0.78	2.48	4.70	K0.0 III	4602 \pm 57
337	β And	2.05	1.24	3.88	12.63	M0.0 III	3763 \pm 46
603	γ_1 And	2.10	0.94	2.91	6.66	K3.0 II	4253 \pm 52
617	α Ari	2.00	0.84	2.64	6.33	K2.0 III	4493 \pm 55
643	60 And	0.00	K3.5 III	...
834	η Per	3.79	1.23	3.70	3.17	K3.0 I	4257 \pm 53
843	17 Per	4.53	1.21	3.75	1.14	K7.0 III	3799 \pm 47
911	α Cet	2.53	1.35	4.21	9.57	M3.0 III	3578 \pm 53
921	ρ Per	3.39	1.80	5.32	10.58	M4.0 II	3281 \pm 40
1017	α Per	1.79	0.45	1.23	7.03	F5.0 I	6750 \pm 85
1231	γ Eri	2.94	1.26	3.87	5.45	M0.5 III	3703 \pm 54
1373	δ_1 Tau	3.76	0.73	2.12	1.05	K0.0 III	4897 \pm 65
1409	ϵ Tau	3.54	0.73	2.21	1.31	G9.5 III	4843 \pm 62
1457	α Tau	0.86	1.23	3.67	33.31	K5.0 III	3871 \pm 48
1577	ι Aur	2.69	1.06	3.32	5.22	K3.0 II	4086 \pm 50
1601	π_6 Ori	4.49	1.05	...	0.93	K2.0 II	4361 \pm 66
1605	ϵ Aur	2.99	0.52	1.53	3.66	F0.0 I	7071 \pm 165
2091	π Aur	4.25	1.69	5.10	4.51	M3.0 II	3489 \pm 43
2216	η Gem	3.28	1.49	4.59	6.65	M3.0 III	3462 \pm 43
2286	μ Gem	2.87	1.57	4.76	11.21	M3.0 III	3483 \pm 43
2473	ϵ Gem	2.98	0.96	2.76	2.98	G8.0 I	4485 \pm 55
2491	α CMa	-1.46	0.00	-0.15	119.20	A1.0 V	9991 \pm 144
2943	α CMi	0.37	0.42	1.01	18.22	F5.0 IV	6553 \pm 81
2990	β Gem	1.14	0.75	2.23	11.82	K0.0 III	4858 \pm 60
3249	β Cnc	3.53	1.12	3.37	2.37	K4.0 III	4012 \pm 52
3576	ρ UMa	4.76	1.47	4.47	...	M3.0 III	...
3705	α Lyn	3.13	1.23	3.74	4.10	K7.0 III	3836 \pm 47
3748	α Hya	1.97	1.04	3.16	8.56	K3.0 II	4060 \pm 50
3873	ϵ Leo	2.98	0.65	1.83	1.86	G1.0 II	5391 \pm 102
4069	μ UMa	3.05	1.28	3.93	5.02	M0.0 III	3793 \pm 47
4301	α UMa	1.79	0.81	2.44	6.99	K0.0 III	4637 \pm 62
4335	ψ UMa	3.01	0.84	2.57	2.42	K1.0 III	4550 \pm 56
4377	ν UMa	3.49	1.06	3.18	2.11	K3.0 III	4091 \pm 50
4434	λ Dra	3.85	1.31	3.99	2.51	M0.0 III	3675 \pm 46
4517	ν Vir	4.04	1.26	3.96	2.12	M1.0 III	3610 \pm 53
4910	δ Vir	3.38	1.53	4.63	6.43	M3.0 III	3602 \pm 44
4932	ϵ Vir	2.84	0.64	2.04	2.21	G8.0 III	4981 \pm 61

Table 4—Continued

HR	Name	V	$(V - R)$	$(V - K)$	Flux (nW/m ²)	Spectral Type	$T_{\text{EFF}}(K)$
5235	η Boo	2.68	0.44	1.31	2.17	G0.0 IV	5964 \pm 75
5340	α Boo	-0.05	0.97	2.95	48.56	K1.0 III	4226 \pm 53
5563	β UMi	2.08	1.11	...	7.76	K4.0 III	3849 \pm 47
5589	R UMi	4.59	1.86	5.54	4.33	M5.0 III	3281 \pm 45
5602	β Boo	3.50	0.65	2.16	1.25	G8.0 III	4969 \pm 86
5681	δ Boo	3.49	0.73	2.27	1.41	G8.0 III	4850 \pm 60
5854	α Ser	2.64	0.81	2.58	3.38	K2.0 III	4558 \pm 56
6056	δ Oph	2.75	1.29	3.97	7.00	M0.5 III	3721 \pm 47
6132	η Dra	2.74	0.61	2.15	2.50	G8.0 III	4826 \pm 71
6134	α Sco	0.91	M1.5 I	...
6146	30 Her	5.01	2.52	7.02	9.93	M6.0 III	3008 \pm 37
6148	β Her	2.77	0.64	2.17	2.45	G7.0 III	4979 \pm 61
6212	ζ Her	2.81	0.51	1.51	2.02	G0.0 IV	5738 \pm 90
6220	η Her	3.50	0.67	2.15	1.26	G8.0 III	4841 \pm 63
6406	α_1 Her	0.00	M5.0 I	...
6418	π Her	3.16	0.96	3.18	2.75	K3.0 II	4151 \pm 54
6536	β Dra	2.78	0.68	2.01	2.38	G2.0 II	5118 \pm 71
6623	μ Her	3.42	0.53	1.65	1.25	G5.0 IV	5603 \pm 84
6695	θ Her	3.87	0.90	2.84	1.22	K1.0 II	4367 \pm 54
6705	γ Dra	2.22	1.14	3.56	8.40	K5.0 III	4013 \pm 52
7001	α Lyr	0.03	-0.04	0.01	30.14	A0.0 V	9657 \pm 119
7139	δ_2 Lyr	4.30	1.78	5.53	5.45	M4.0 II	3330 \pm 44
7157	13 Lyr	4.00	2.05	6.09	10.97	M5.0 III	3174 \pm 41
7310	δ Dra	3.07	0.70	2.27	1.95	G9.0 III	4851 \pm 67
7405	α Vul	4.45	1.21	3.90	1.34	M0.0 III	3769 \pm 46
7417	β_1 Cyg	3.08	0.87	2.92	2.92	K3.0 II	4401 \pm 54
7525	γ Aql	2.72	1.07	3.31	4.97	K3.0 II	4099 \pm 50
7536	δ Sge	3.83	1.44	...	3.93	M2.0 II	3446 \pm 45
7557	α Aql	0.76	0.14	0.50	11.72	A7.0 V	7361 \pm 91
7635	γ Sge	3.47	1.20	3.63	2.86	M0.0 III	3859 \pm 48
7735	31 Cyg	3.80	0.97	3.31	2.33	K2.0 II	4377 \pm 54
7751	32 Cyg	3.98	1.20	3.82	2.16	K3.0 I	3855 \pm 47
7796	γ Cyg	2.23	0.49	1.51	6.12	F8.0 I	6703 \pm 83
7924	α Cyg	1.25	0.11	0.36	45.97	A2.0 I	12390 \pm 208
7948	γ_2 Del	3.91	0.68	K1.0 IV	...
7949	ϵ Cyg	2.46	0.73	2.35	3.63	K0.0 III	4756 \pm 59
8079	ξ Cyg	3.70	1.20	3.75	2.88	K4.0 I	4007 \pm 49
8115	ζ Cyg	3.20	0.70	2.11	1.66	G8.0 III	5002 \pm 62

Table 4—Continued

HR	Name	V	$(V - R)$	$(V - K)$	Flux (nW/m ²)	Spectral Type	$T_{\text{EFF}}(K)$
8225	2 Peg	4.57	1.25	...	1.15	M1.0 III	3609 \pm 45
8308	ϵ Peg	2.39	1.05	3.20	5.90	K2.0 I	4224 \pm 85
8316	μ Cep	4.17	2.10	5.82	14.46	M2.0 I	3181 \pm 52
8414	α Aqr	2.93	0.66	1.97	2.02	G2.0 I	4907 \pm 70
8465	ζ Cep	3.35	1.08	3.24	3.27	K1.5 I	4351 \pm 54
8667	λ Peg	3.94	0.76	2.29	0.93	G8.0 III	4699 \pm 71
8684	μ Peg	3.48	0.68	2.05	1.30	G8.0 III	5003 \pm 69
8698	λ Aqr	3.79	1.42	4.49	3.92	M2.5 III	3639 \pm 47
8775	β Peg	2.42	1.50	4.63	15.22	M2.5 II	3448 \pm 42
8796	56 Peg	4.77	0.97	...	0.54	G8.0 I	4152 \pm 65

Table 5. Comparison with Intensity Interferometer Diameters

Star		Limb-darkened		Uniform disk			
HR	Name	Int.	Inter.	Mark III	Int.	Inter.	Mark III
2491	α CMa	5.89 ± 0.16		5.993 ± 0.108	5.60 ± 0.15		5.421 ± 0.255
2943	α CMi	5.50 ± 0.17		5.446 ± 0.054	5.10 ± 0.16		5.302 ± 0.106
7001	α Lyr	3.24 ± 0.07		3.225 ± 0.032	3.08 ± 0.07		2.975 ± 0.059
7557	α Aql	2.98 ± 0.14		3.462 ± 0.035	2.78 ± 0.13		3.115 ± 0.062

Table 6. Comparison of Measured Diameters with Model Atmosphere Diameters

HR	Name	Diameter (mas)		$\Delta\theta$	$\Delta\theta/\sigma$	ref ^a
		Mark III	IRFM			
165	δ And	4.136 ± 0.041	4.131	−0.005	−0.12	1
			4.174	0.038	0.93	3
337	β And	13.749 ± 0.137	13.562	−0.187	−1.36	3
617	α Ari	6.827 ± 0.078	6.910	0.083	1.06	2
911	α Cet	13.238 ± 0.256	12.994	−0.244	−0.95	3
1017	α Per	3.188 ± 0.035	3.238	0.050	1.43	3
1373	δ^1 Tau	2.338 ± 0.033	2.262	−0.076	−2.30	3
			2.269	−0.069	−2.09	1
1409	ϵ^2 Tau	2.671 ± 0.032	2.594	−0.077	−2.41	3
			2.640	−0.031	−0.97	2
1457	α Tau	21.099 ± 0.211	20.620	−0.479	−2.27	2
			21.154	0.055	0.26	3
2473	ϵ Gem	4.703 ± 0.047	4.775	0.072	1.53	3
			4.769	0.066	1.40	1
2990	β Gem	7.980 ± 0.080	7.968	−0.012	−0.15	3
			8.028	0.048	0.60	1
			8.040	0.060	0.75	2
3249	β Cnc	5.238 ± 0.069	5.170	−0.068	−0.99	2
3748	α Hya	9.727 ± 0.097	9.440	−0.287	−2.96	2
3873	ϵ Leo	2.575 ± 0.078	2.720	0.145	1.86	2
4301	α UMa	6.739 ± 0.099	6.790	0.051	0.52	2
4335	ψ UMa	4.120 ± 0.041	4.180	0.060	1.46	2
4932	ϵ Vir	3.283 ± 0.033	3.300	0.017	0.52	2
5235	η Boo	2.269 ± 0.025	2.237	−0.032	−1.28	3
			2.210	−0.059	−2.36	1
			2.260	−0.009	−0.36	2
5340	α Boo	21.373 ± 0.247	21.070	−0.303	−1.23	2
			20.927	−0.446	−1.81	3
5602	β Boo	2.477 ± 0.065	2.461	−0.016	−0.25	1
			2.610	0.133	2.05	2
			2.469	−0.008	−0.12	3
5681	δ Boo	2.764 ± 0.030	2.769	0.005	0.17	1

Table 6—Continued

HR	Name	Diameter (mas)		$\Delta\theta$	$\Delta\theta/\sigma$	ref ^a
		Mark III	IRFM			
			2.800	0.036	1.20	2
			2.749	−0.015	−0.50	3
5854	α Ser	4.846 ± 0.048	4.960	0.114	2.38	2
			4.796	−0.050	−1.04	3
6056	δ Oph	10.471 ± 0.117	10.179	−0.292	−2.50	3
6132	η Dra	3.722 ± 0.071	3.438	−0.284	−4.00	1
			3.462	−0.260	−3.66	3
6148	β Her	3.462 ± 0.035	3.481	0.019	0.54	1
			3.455	−0.007	−0.20	3
6220	η Her	2.624 ± 0.034	2.610	−0.014	−0.41	2
6418	π Her	5.275 ± 0.067	5.520	0.245	3.66	2
6623	μ Her	1.953 ± 0.039	1.956	0.003	0.08	1
			1.990	0.037	0.95	2
			1.966	0.013	0.33	3
6705	γ Dra	9.860 ± 0.128	10.450	0.590	4.61	2
			10.244	0.384	3.00	3
7525	γ Aql	7.271 ± 0.073	7.198	−0.073	−1.00	3
7949	ϵ Cyg	4.612 ± 0.046	4.557	−0.055	−1.20	1
			4.599	−0.013	−0.28	3
8414	α Aqr	3.237 ± 0.057	2.972	−0.265	−4.65	1
			3.002	−0.235	−4.12	3
8684	μ Peg	2.496 ± 0.040	2.503	0.007	0.18	1
			2.470	−0.026	−0.65	2
8775	β Peg	17.982 ± 0.180	17.309	−0.673	−3.74	3

^aReferences. 1: Blackwell & Lynas-Gray (1993) 2: Bell & Gustafsson (1989) 3: Blackwell et al. (1990)

Table 7. Extinction Values

Star	A_V	σ
HR 834	0.83	0.34
HR1017	0.48	0.17
HR1577	0.24	0.15
HR1601	0.46	0.23
HR1605	0.96	0.38
HR2091	0.43	0.17
HR2473	0.21	0.14
HR7525	0.21	0.21
HR7735	0.31	0.15
HR7751	0.23	0.16
HR7796	0.85	0.33
HR7924	1.25	0.58
HR8079	0.48	0.25
HR8316	1.80	0.65
HR8465	0.62	0.25

REFERENCES

- Arenou, F., Grenon, M., & Gomez, A. 1992, A&A, 258, 104
- Barnes, T. G., & Evans, D. S. 1976, MNRAS, 174, 489
- Bell, R. A., & Gustafsson, B. 1989, MNRAS, 236, 653
- Blackwell, D. E., & Lynas-Gray, A. E. 1993, A&A, 282, 899
- Blackwell, D. E., & Shallis, M. J. 1977, MNRAS, 180, 177
- Blackwell, D. E., Petford, A. D., Arribas, S., Haddock, D. J., & Shelby, M. J. 1990, A&A, 232, 396
- Cardelli, J. A., Clayton, G. C., & Mathis, J. S. 1989, ApJ, 45, 245
- Claret, A., Diaz-Cordoves, J., & Gimenez, A. 1995, A&AS, 114, 247
- Code, A. D., Holm, A. V., & Bottemiller, R. L. 1980, ApJS, 43, 501
- Cohen, M., Walker, R. G., Barlow, M. & Deacon, J. R. 1992, AJ, 104, 1650
- Di Benedetto, G. P. & Rabbia Y. 1987 A&A, 188, 114
- Di Benedetto G. P. & Ferluga, S. 1990 A&A 236, 449
- Di Benedetto G. P. & Foy, R. 1986 A&A 166, 204
- Diaz-Cordoves, J., Claret, A., & Gimenez, A. 1995, A&AS, 110, 329
- Dyck, H. M., Benson, J. A., van Belle, G. T., & Ridgway, S. T. 1996, AJ, 111, 1705
- Fouqué, P., & Gieren, W. P. 1997, A&A, 320, 799
- Gray, R. O., & Napier, M. G. 2001, AJ, 121, 2148
- Hajian, A. R., Armstrong, J. T., Hummel, C. A., Benson, J. A., Mozurkewich, D., Pauls, T. A., Hutter, D. J., Elias II, N. M., Johnston, K. J., Rickard, L. J., & White, N. M. 1998, ApJ, 496, 484
- Hutter, D. J., Johnston, K. J., Mozurkewich, D., Simon, R. S., Colavita, M. M., Pan, X. P., Shao, M., Hines, B. E., Staelin, D. H., Hershey, J. L., Hughes, J. A., & Kaplan, G. H. 1989, ApJ, 340, 1103
- Hanbury Brown, R., Davis, J., & Allen, L. R. 1974, MNRAS, 167, 121
- Hayes, D. S., & Latham, D. W. 1975, ApJ, 197, 593
- Hindsley, R. B., & Bell, R. A. 1989, ApJ, 341, 1004

- Hoffleit, D. 1990, *The Bright Star Catalog* Yale University Observatory, New Haven
- Johnson, H. L., Iriarte, B., Mitchell, R. I., & Wisniewskj, W. Z. 1966, *Comm. Lunar Plan. Lab.*, 4, 99.
- Mozurkewich, D., Johnston, K. J., Simon, R. S., Bowers, P. F., Gaume, R., Hutter, D. J., Colavita, M. M., Shao, M., & Pan, X. P. 1991, *AJ*, 101, 2207
- Nordgren, T. E., Germain, M. E., Benson, J. A., Mozurkewich, D., Sudol, J. J., Elias II, N. M., Hajian, A. R., White, N. M., Hutter, D., J., Johnston, K. J., Gauss, F. S., Armstrong, J. T., Pauls, T. A., & Rickard, L. J 1999, *AJ*, 118, 3032
- Nordgren, T. E., Sudol, J. J., & Mozurkewich, D., 2001 *AJ*, 122, 270
- Quirrenbach, A., Mozurkewich, D., Armstrong, J. T., Johnston, K. J., Colavita, M. M., & Shao, M. 1992, *A&A*, 259, L19
- Quirrenbach, A., Mozurkewich, D., Armstrong, J. T., Buscher, D. F., & Hummel, C. A. 1993, *ApJ*, 406, 215
- Quirrenbach, A., Mozurkewich, D., Hummel, C. A., Buscher, D. F., & Armstrong, J. T. 1994a, *A&A*285, 541
- Quirrenbach, A., Mozurkewich, D., Buscher, D. F., Hummel, C. A., & Armstrong, J. T. 1994b, *A&A*286, 1019
- Quirrenbach, A., Mozurkewich, D., Buscher, D. F., Hummel, C. A., & Armstrong, J. T. 1996, *A&A*, 312, 160
- Ridgway, S. T., Jacoby, G. H., Joyce, R. R., Siegel, M. J., & Wells, D. C. 1982, *AJ*, 87, 1044
- Shao, M., Colavita, M. M., Hines, B. E., Staelin, D. H., Hutter, D. J., Johnston, K. J., Mozurkewich, D., Simon, R. S., Hershey, J. L., Hughes, J. A., & Kaplan, G. H. 1988a, *A&A*, 193, 357
- Shao, M., Colavita, M. M., Hines, B. E., Staelin, D. H., Hutter, D. J., Johnston, K. J., Mozurkewich, D., Simon, R. S., Hershey, J. L., Hughes, J. A., & Kaplan, G. H. 1988b, *ApJ*, 327, 905
- Straizys, V. 1992, *Multicolor Stellar Photometry*, Pachart Publishing House, Tucson
- Tug, H., White, N. M., & Lockwood, G. W. 1977, *A&A*, 61, 679
- ESA 1997, *The Hipparcos and Tycho Catalogues*, ESA SP-1200
- Welty, D. E. & Hobbs, L. M. 2001, *ApJS*133, 345
- van Belle, G. T., Lane, B. F., Thompson, R. R., Boden, A. F., Colavita, M. M., Dumont, P. J., Mobley, D. W., Palmer, D., Shao, M., Vasisht, G. X., Wallace, J. K., Creech-Eakman, M. J., Koresko, C. D., Kulkarni, S. R. Pan, X. P., & Gubler, J. 1999a, *AJ*, 117, 521

van Belle, G. T. 1999b, *PASP*, 111, 1515

van Belle, G. T., Ciardi, D. R., Thompson, R. R., Akeson, R. L. , Lada, E. A. 2001, *ApJ*559, 1155

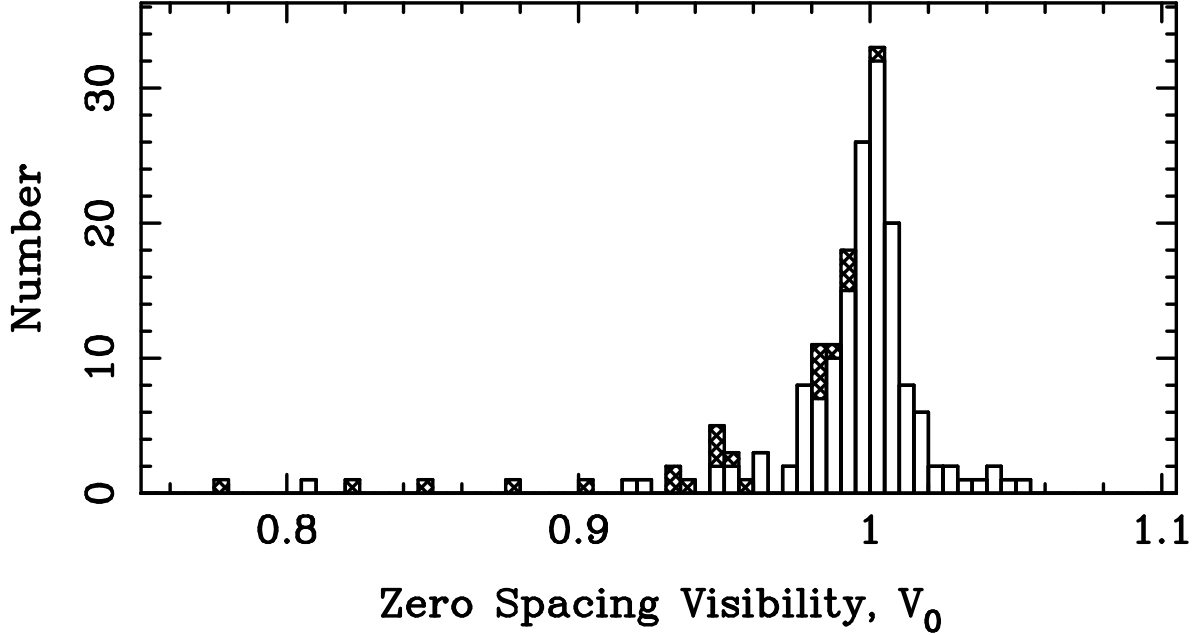


Fig. 1.— Histogram of the zero spacing visibility amplitude, V_0 , determined from two-parameter fits to visibility data. The tail toward low values of V_0 demonstrates that a one-parameter uniform disk model is not always sufficient to fit the data. If there is a stellar companion close enough to the primary to contribute flux to the detector but distant enough so that the fringe packets do not overlap, the visibility amplitude will be reduced. The cross-hatched entries are the known binaries. The non-binary with low V_0 is μ Cep, a supergiant that apparently also has significant emission at scales too large to be sampled by our shortest baseline. After the binaries and μ Cep are removed, the histogram is symmetric with a mean value of 0.996 and a standard deviation of 0.018.

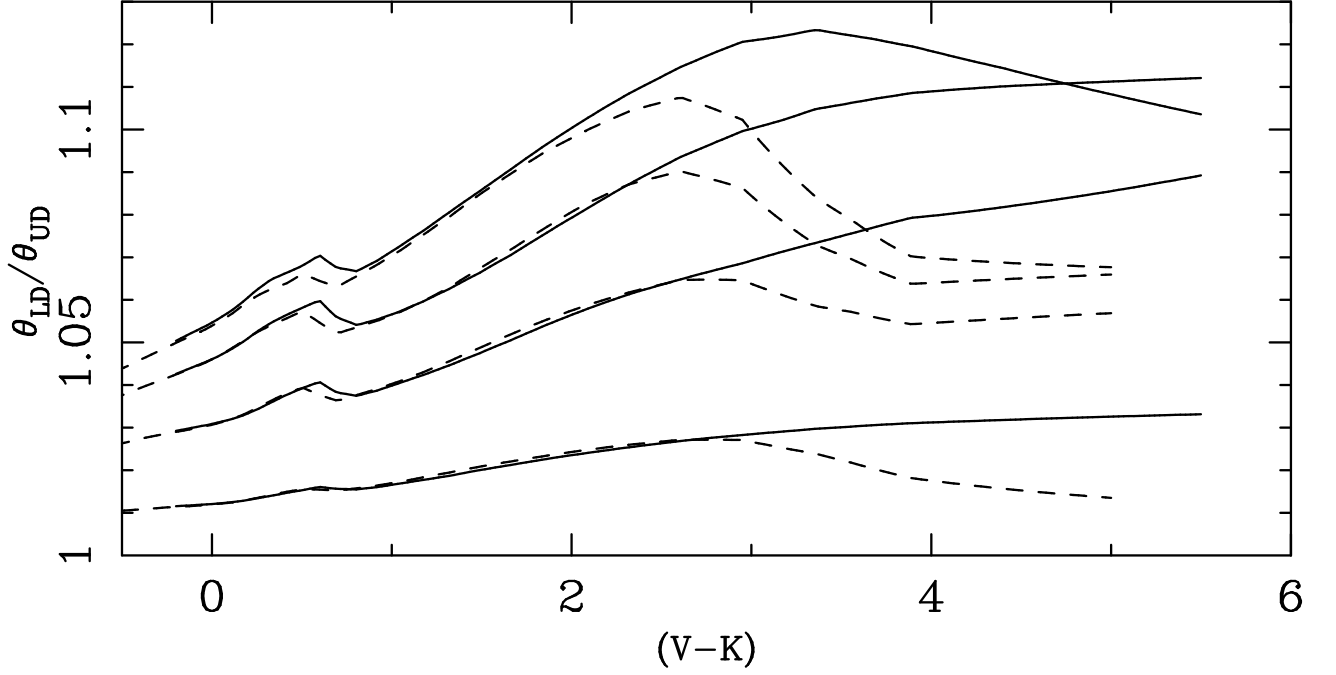


Fig. 2.— Limb-darkening conversion factors versus $(V - K)$. The dashed curves are for main sequence stars; the solid curves are for giants. From top to bottom, the curves show conversion factors for 451 nm, 550 nm, 800 nm and $2.2 \mu\text{m}$. It is not possible to determine the stars’ intensity profiles from the data presented in this paper. As a result, we fit uniform-disk diameters to the data and convert them to limb-darkened diameters using model atmospheres. This figure shows how that limb-darkening conversion varies with the type of star and with wavelength.

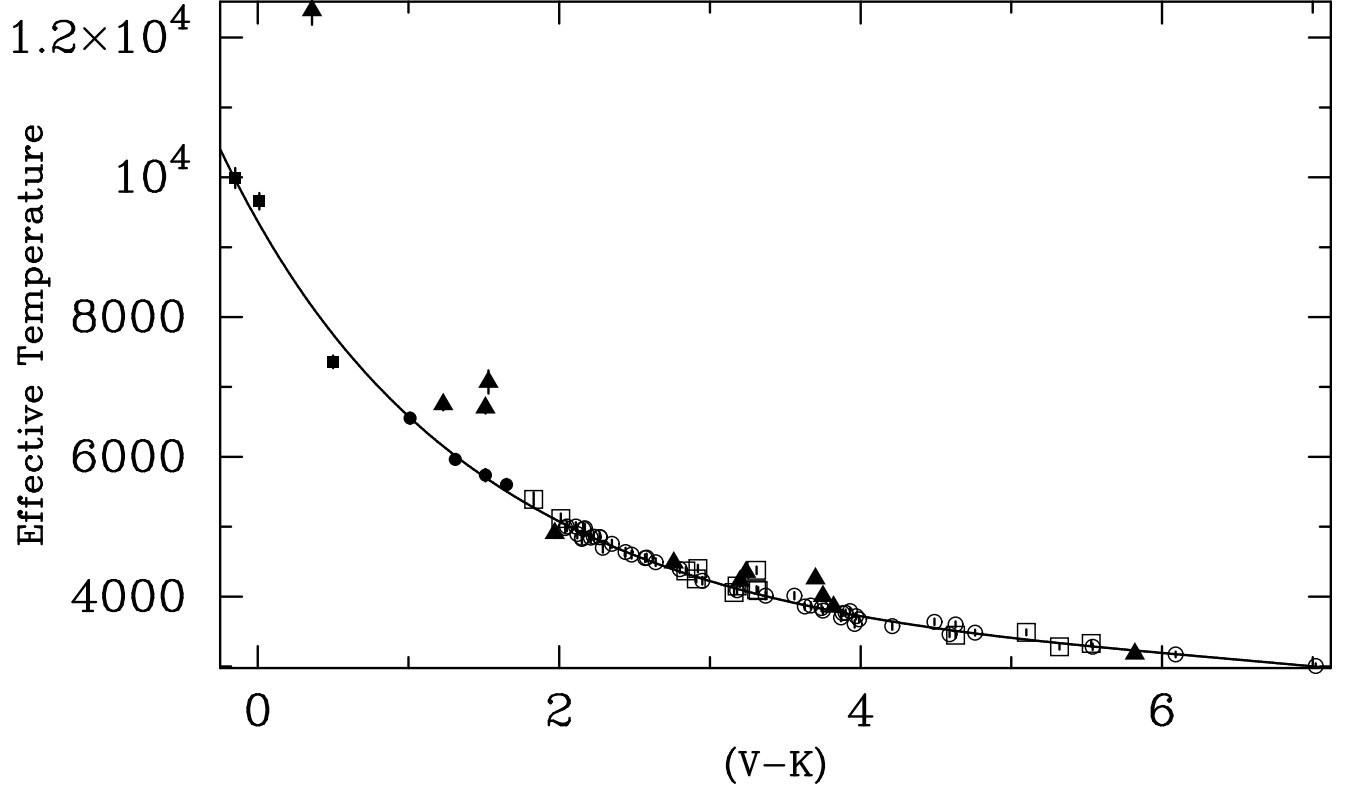


Fig. 3.— Plot of measured effective temperatures as a function of $(V - K)$. The markers indicate different luminosity classes: I triangle, II open square, III open circle, IV filled circle and V filled square. The outliers are all supergiants and are four of the five highest extinction stars in the sample. Their departure from the distribution is probably due to poor extinction corrections (see text). The curve is a fit to the low-extinction stars and is quadratic in the log of the temperature.

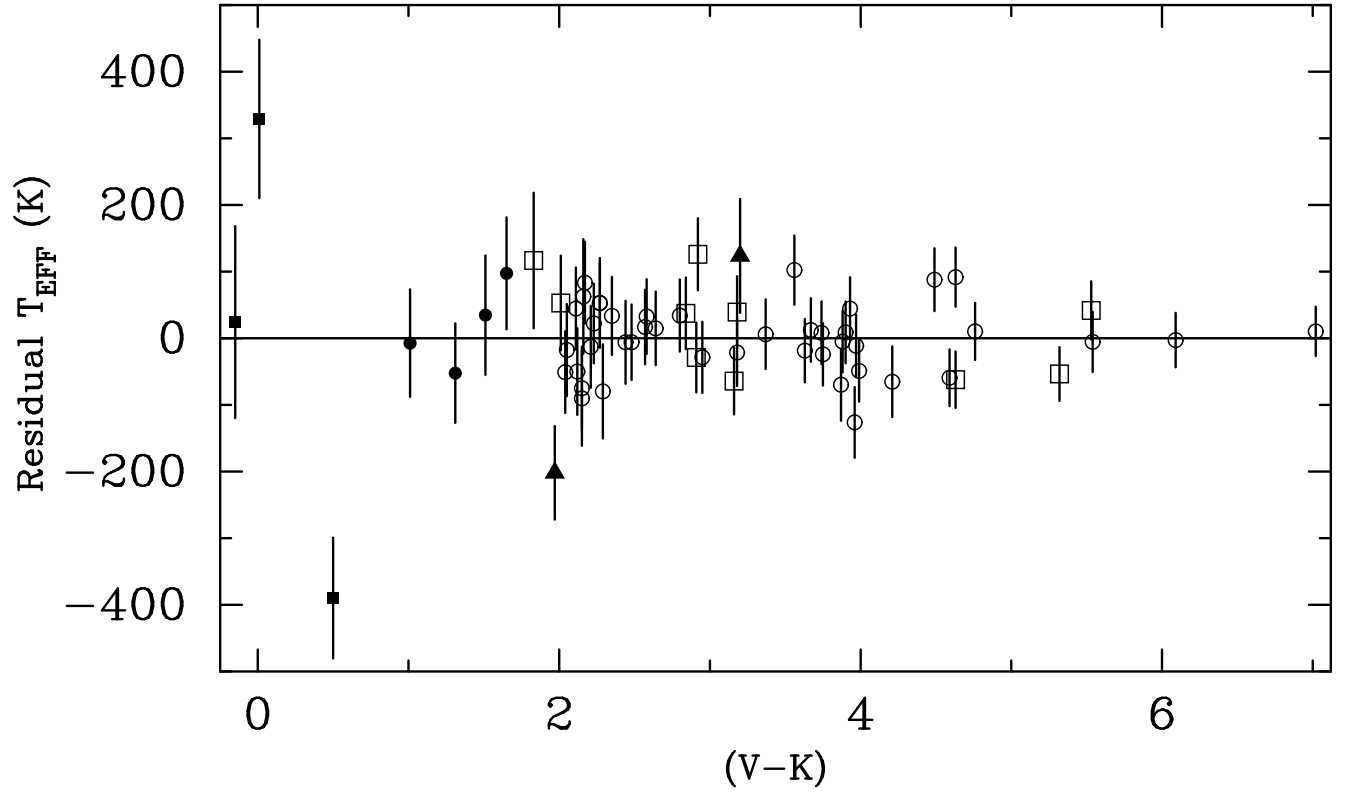


Fig. 4.— Difference between the measured effective temperatures and the fit shown in Figure 3. The symbols are the same as in Figure 3. Considering only the low-extinction stars, the scatter is less than 100K rms when all luminosity classes are included and about 50K when only the giants are included.

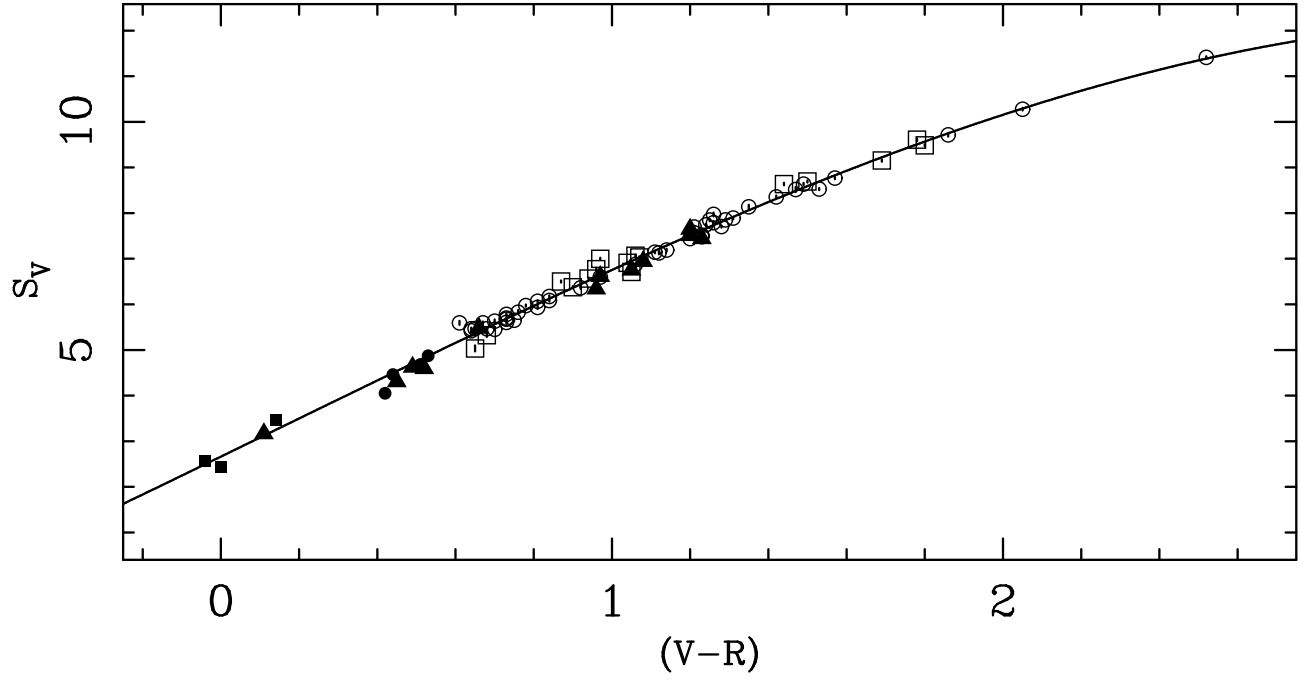


Fig. 5.— Surface brightness, $S_V = m_V + 5 \log_{10}(\theta)$, where θ is the angular diameter in milliarcseconds, versus Johnson $(V - R)$. The symbols represent luminosity class and are the same as in Figure 3. The line is the cubic fit specified by Equation 6.

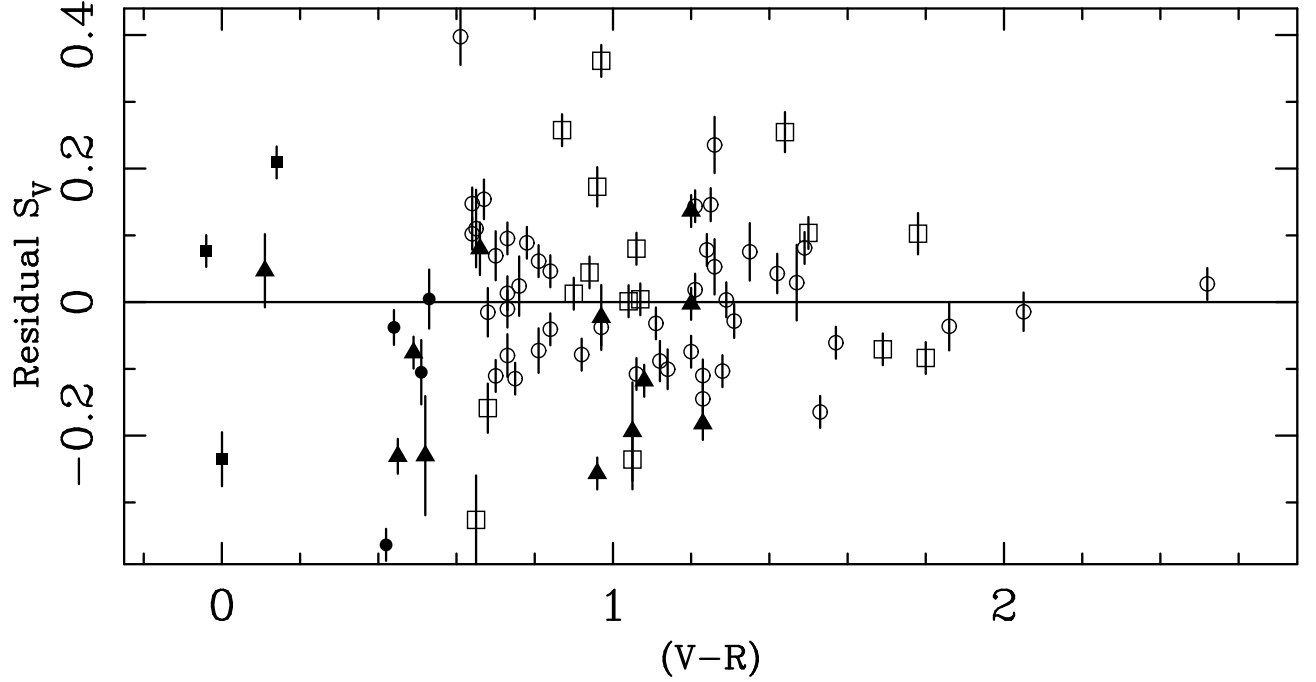


Fig. 6.— Residuals between the data and fit shown in Figure 5. As in previous figures, the symbols represent luminosity class and are the same as in Figure 3. The scatter is larger than can be explained by the uncertainties in either the angular diameters or the photometry and is probably intrinsic to the relationship.

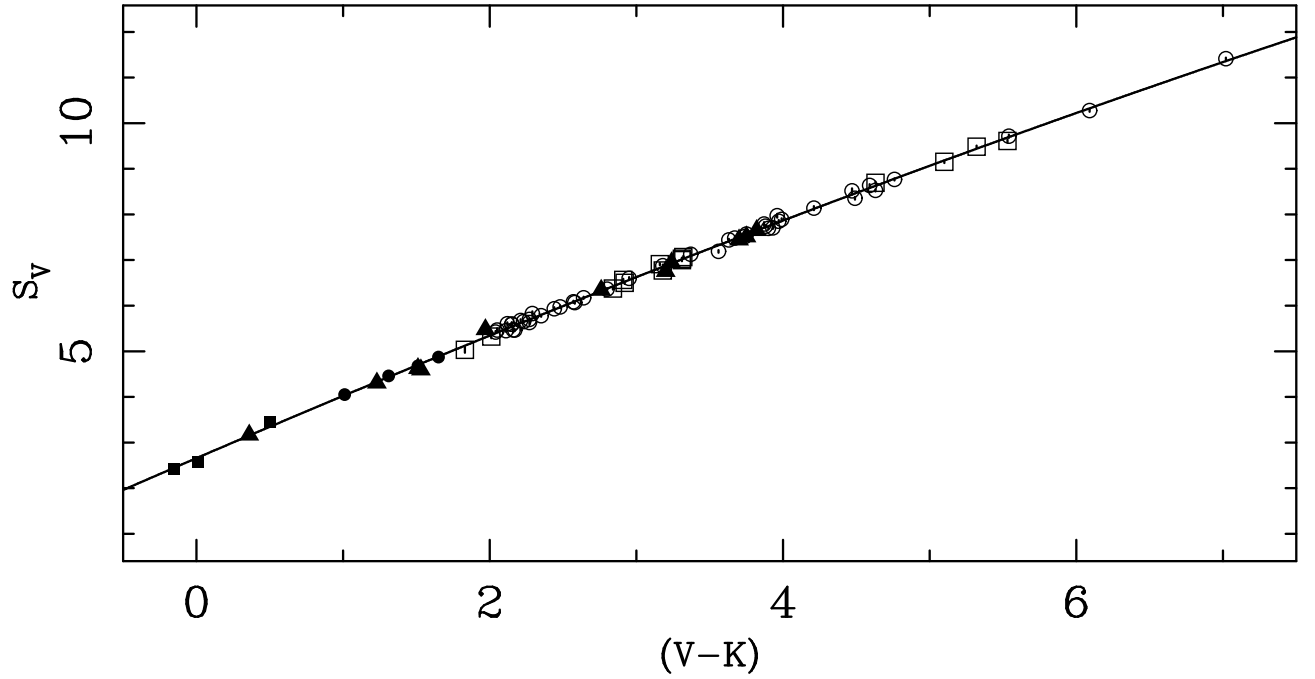


Fig. 7.— Surface brightness versus $(V - K)$. Using $(V - K)$ as the surrogate for temperature produces a relationship where the reddening curve is almost parallel to the surface brightness relationship, making this useful for estimating stellar angular diameters. The scatter implies that angular diameter estimates are good to about 3%. The symbols represent luminosity class and are the same as in Figure 3. The line is the quadratic fit given by Equation 7.

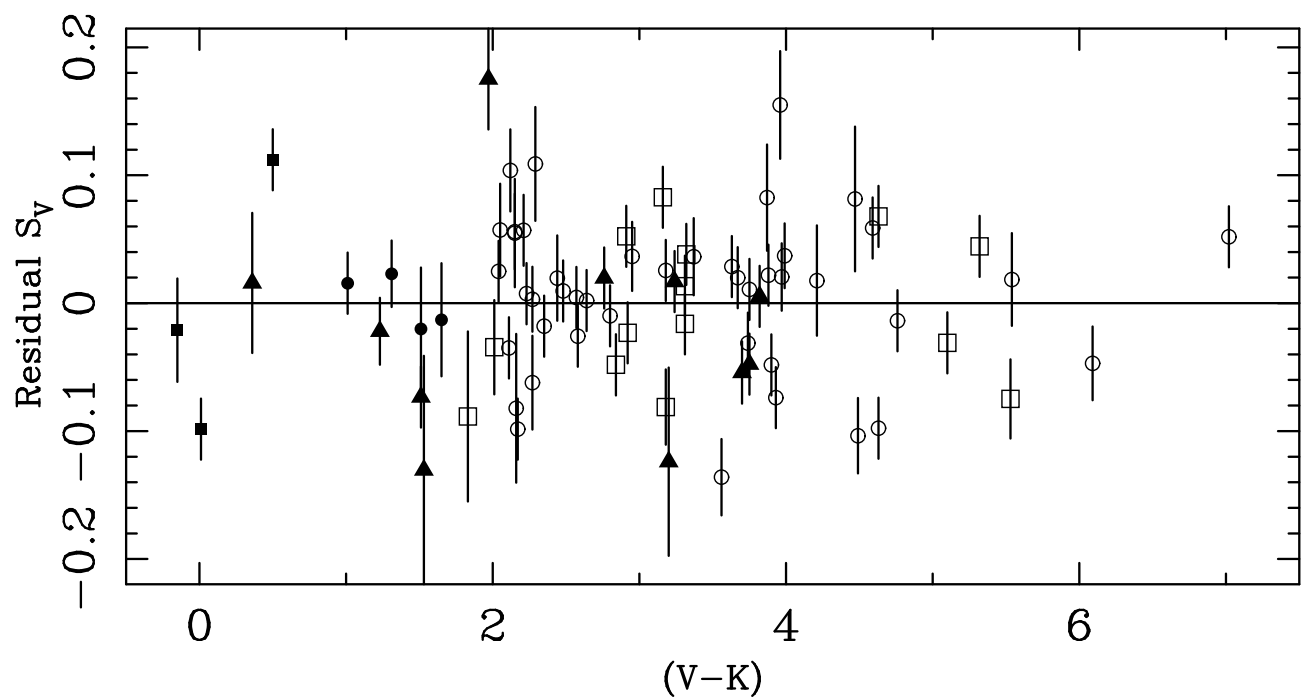


Fig. 8.— Residuals of the surface brightness versus $(V - K)$ data to the fit shown in Figure 7.

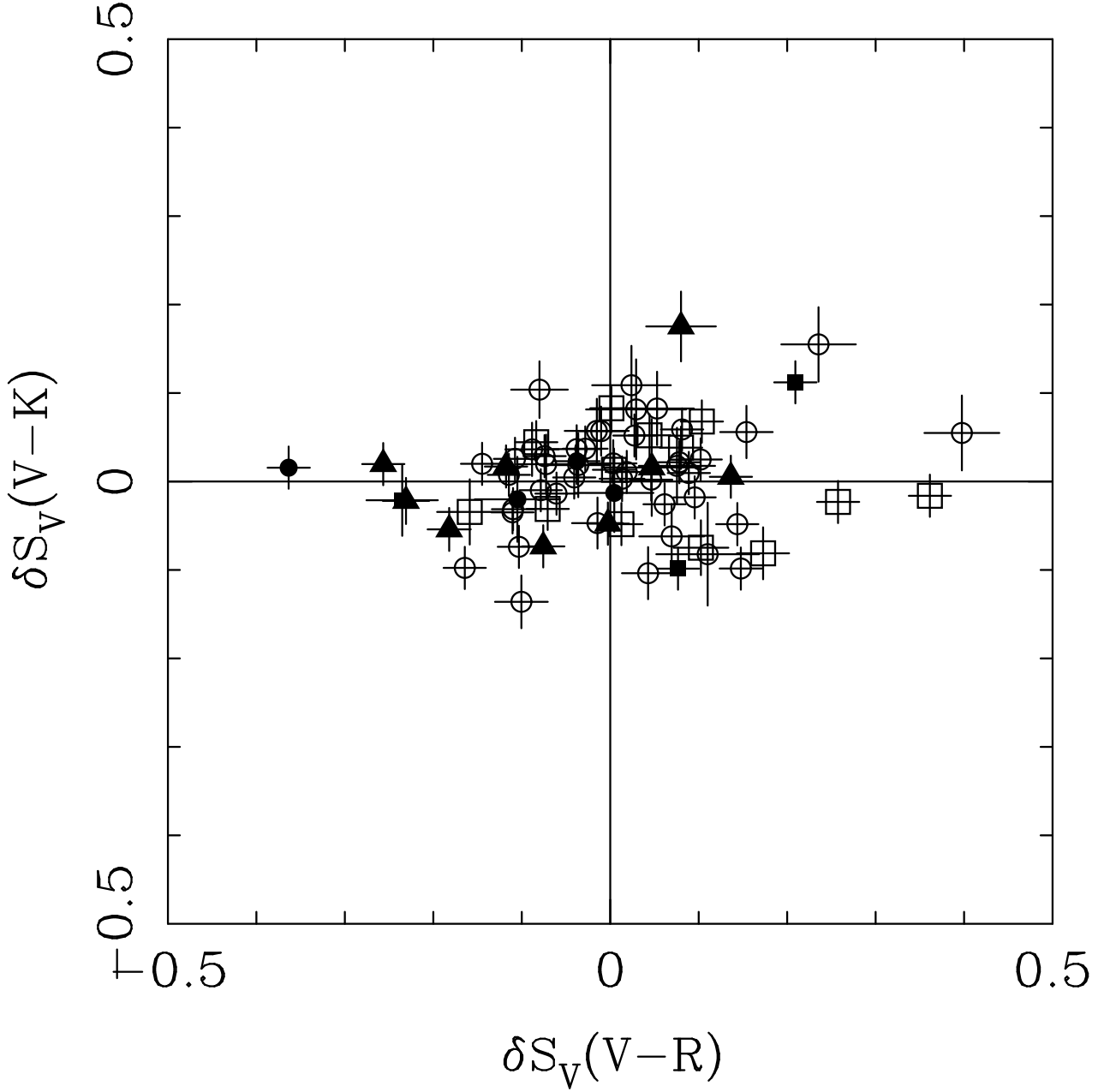


Fig. 9.— Residuals of $S_V(V - K)$ versus the residuals of $S_V(V - R)$. The correlation coefficient is 0.17, implying that the uncorrelated noise has a variance 1.8 times larger than the correlated noise. If the scatter in these relationships were primarily in either the angular diameters or the V magnitudes, the variance of the correlated noise would be larger than the variance of the uncorrelated noise. We use this lack of correlation to argue that the scatter in Figures 5 and 7 is not in the measurements but is intrinsic to the surface brightness relationships. Again, the symbols, indicating luminosity class, are the same as in Figure 3.

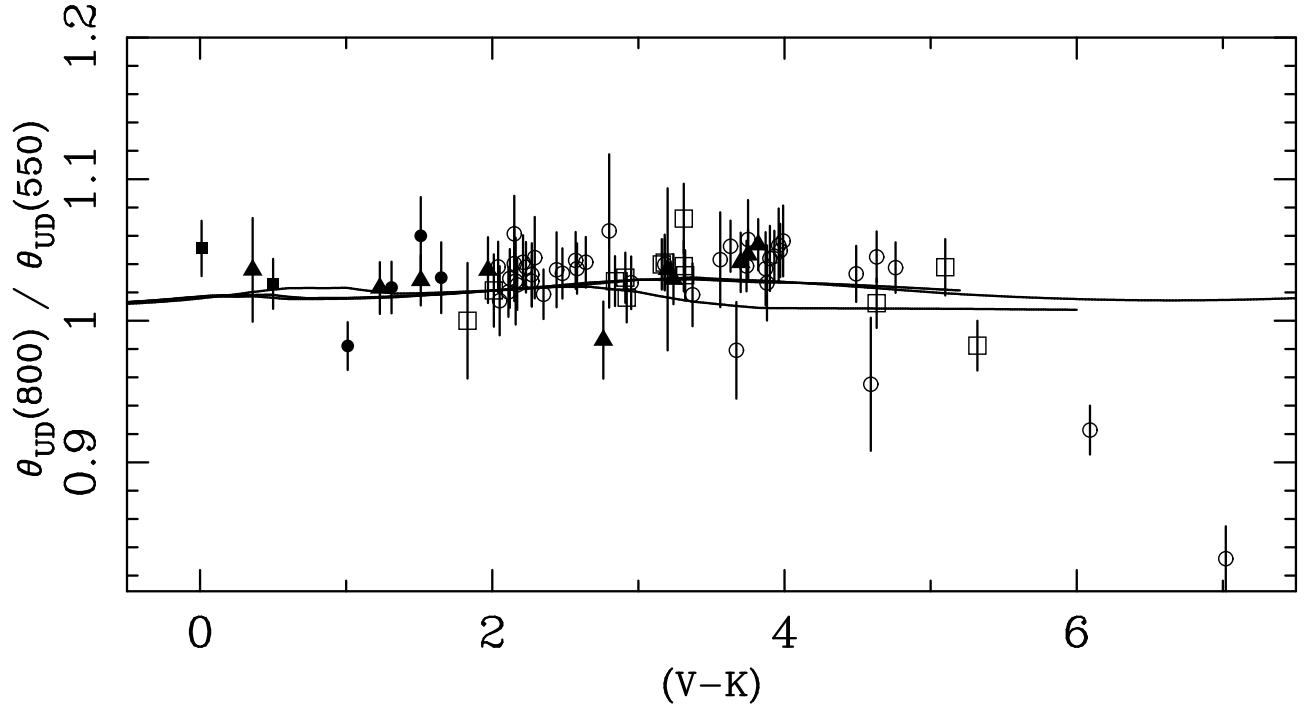


Fig. 10.— The ratio of the uniform disk angular diameter measured at 800 nm to that measured at 550 nm. The vertical lines represent 1σ errors. The three curves show the effect of the wavelength dependence of limb darkening and are from model atmosphere calculations by Kurucz for main sequence, giants and supergiants. The symbols represent luminosity class and are the same as in Figure 3.

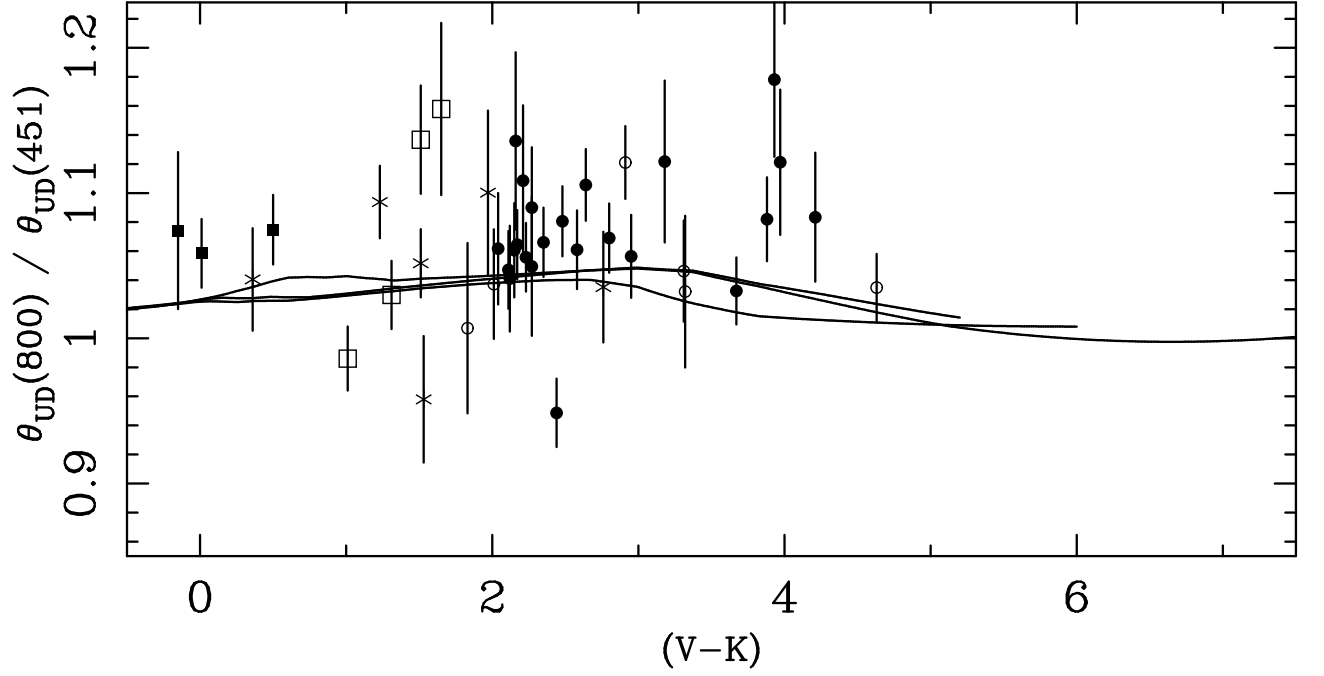


Fig. 11.— The ratio of the uniform disk angular diameter measured at 800 nm divided by that measured at 451 nm. As in Figure 10, the curves show the effect of limb darkening. Again, the measured ratios are slightly larger than predicted by the models. The symbols indicate different luminosity classes and are described in Figure 3.

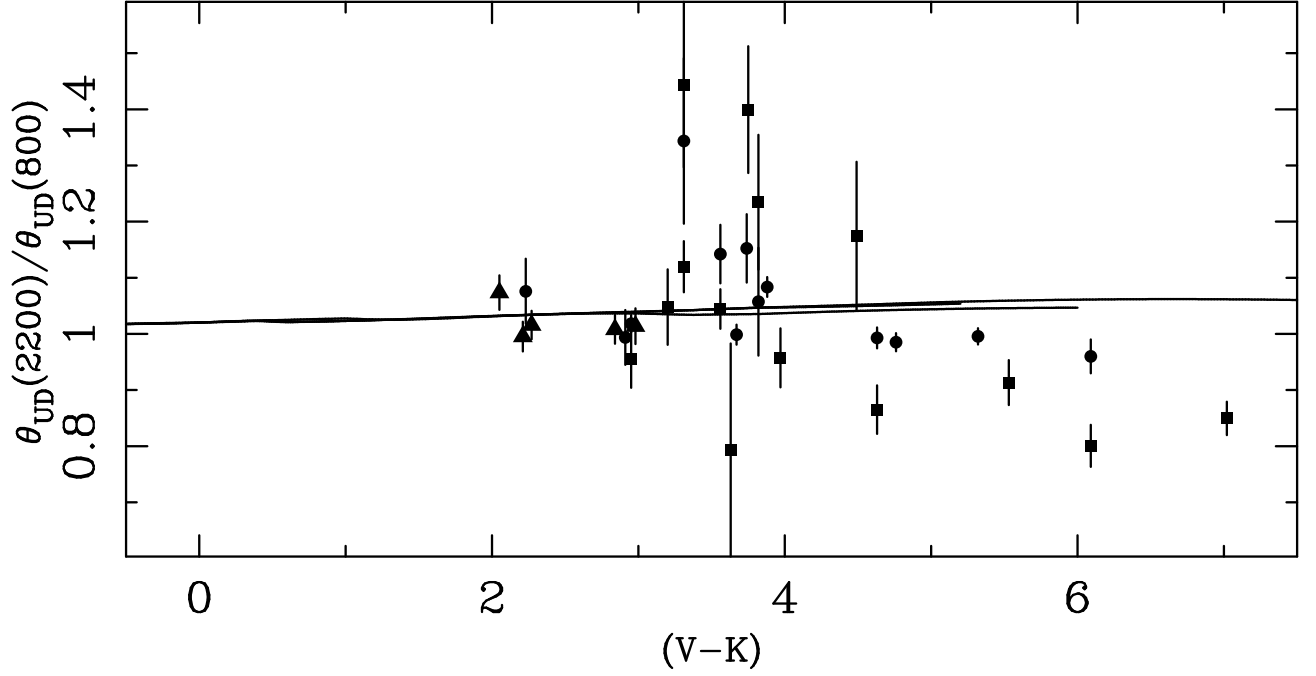


Fig. 12.— The ratio of uniform disk angular diameters at K band to that at 800 nm. The infrared data were taken from I2T (circles), IOTA (squares) and PTI (triangles). The vertical lines indicate the 1σ errors. The horizontal lines are calculations from model atmospheres for main sequence, giants and supergiants.

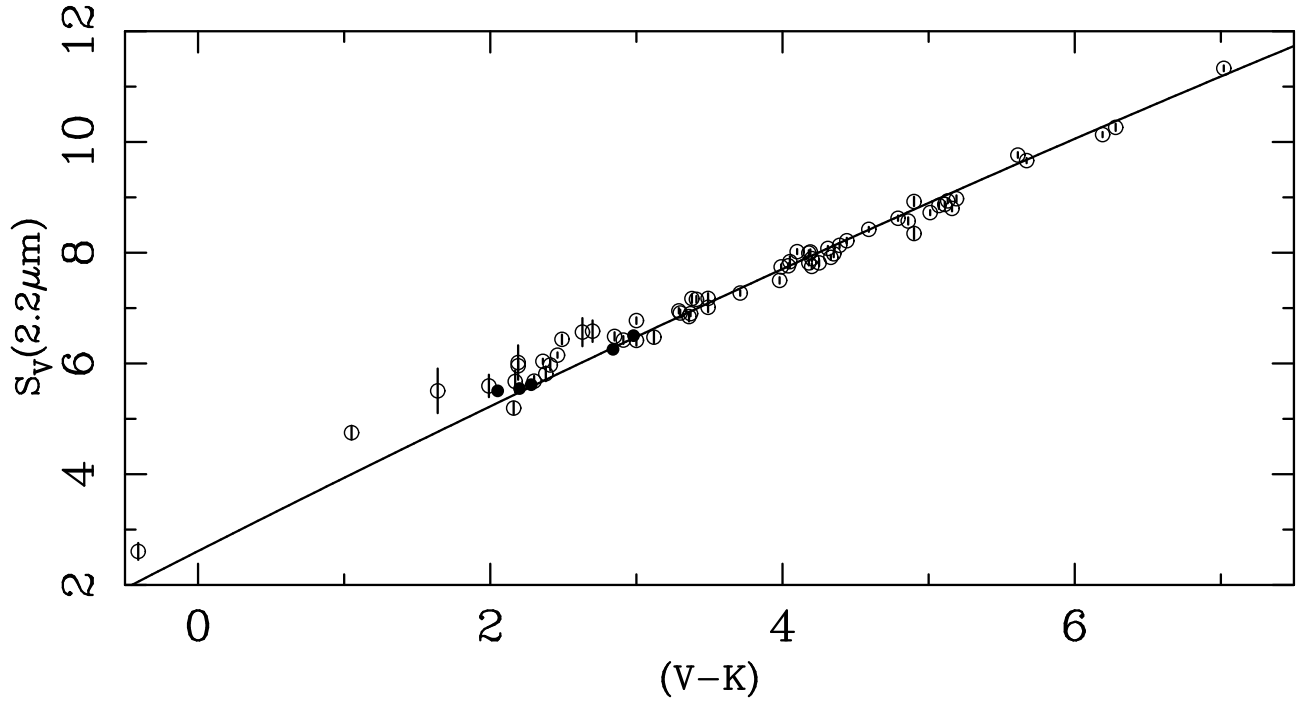


Fig. 13.— Surface brightness versus $(V - K)$ for stars observed by PTI (van Belle et al., 1999a). The surface brightness was generated from the PTI $2.2 \mu\text{m}$ uniform-disk (not limb-darkened) diameters. The solid line is a quadratic fit to the 800 nm surface brightnesses from the Mark III. The difference between the data and the line is five times the logarithm of the ratio of the $2.2 \mu\text{m}$ to 800 nm uniform disk diameters.

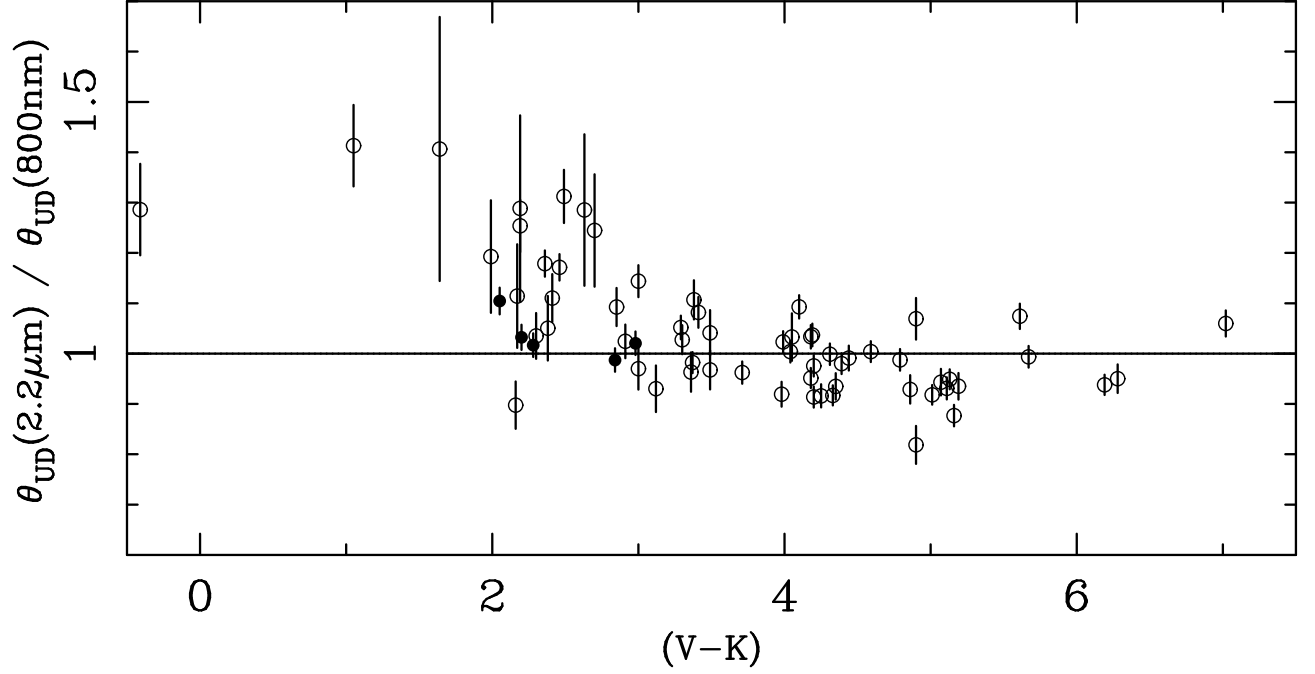


Fig. 14.— The ratio of PTI $2.2\ \mu\text{m}$ uniform disk diameters to the 800 nm uniform disk diameters predicted by Equation 13. The data are the same as those shown in Figure 13. Stars observed by both PTI and the Mark III are shown with filled symbols.